UNIVERSITY OF CALIFORNIA
RIVERSIDE

Iron Isotope and Rare Earth Element Patterns of the Neoproterozoic Fulu Formation, South China: Implications for Late Proterozoic Ocean Chemistry

A Thesis submitted in partial satisfaction
of the requirements for the degree of

Master of Science

in

Geological Sciences

by

Elizabeth Goldbaum

August 2014

Thesis Committee:
Dr. Timothy Lyons, Chairperson
Dr. Noah Planavsky
Dr. Gordon Love

The Thesis of Elizabeth Goldbaum is approved:

_____

_____

_____

Committee Chairperson

University of California, Riverside

ABSTRACT OF THE THESIS

Iron Isotopes and Rare Earth Element Patterns of the
Neoproterozoic Fulu Formation, South China:
Implications for Late Proterozoic Ocean Chemistry

by

Elizabeth Goldbaum

Master of Science, Graduate Program in Geological Sciences
University of California, Riverside, August 2014
Dr. Timothy Lyons, Chairperson

The Neoproterozoic Era, from around 1000 to 570 million years ago, witnessed the widespread deposition of Iron Formations (IFs) in close association with global glaciations. These IFs record distinct iron isotope and rare earth element patterns that allow us to reconstruct their depositional environment. The Fulu Formation of South China is a regional example of a global phenomenon. The Fulu was deposited immediately following the breakup of the Supercontinent Rodinia, which provided a restricted rift basin and contributed to an ample supply of iron. Specifically, iron isotopes and rare earth element profiles point to hydrothermally sourced iron in an oxygen-limited environment as the major driver of deposition for the Fulu Formation.

Table of Contents

1. Introduction

The Neoproterozoic Era witnessed dramatic climatic changes including a global freeze that likely glaciated vast portions of the continents and oceans, even at low elevations and latitudes (Harland 1964; Kirschvink 1992; Hoffman et al., 1998). Plunging temperatures were likely initiated by the breakup of the supercontinent Rodinia, which rapidly pulled carbon dioxide out of the atmosphere through extensive weathering reactions involving newly exposed continental crust (Hoffman 1999). Tied to the widespread glaciations are Iron Formations (IFs), which record the local and regional conditions of deposition and can capture isotopic and elemental records that broadly elucidate seawater chemistry. Neoproterozoic IFs (NIFs) mark a resurgence in large-scale deep water iron deposition following a billion-year-long mid-Proterozoic lull.

Recent research (Planavsky et al. 2011; Poulton and Canfield 2011; Lyons et al. 2014) has indicated the persistence of ferruginous (iron-rich, oxygen depleted) conditions throughout much if not most of the Proterozoic, implying that exceptional and likely episodic iron inputs from glacial and hydrothermal sources were key in stimulating and sustaining NIF formation, with the latter enhanced at times of low sulfate in the ocean (Kump and Seyfried 2005).

NIFs are often associated with glaciogenic lithologies (Klein and Beukes 1993; Klein and Ladeira 2004; Baldwin et al. 2012), and it is generally accepted that the widespread Neoproterozoic glaciations played a key role in the distribution and deposition of these IFs—although the cause-and-effect relationships are not well

understood. Specifically, the environmental conditions, iron sources, and formation mechanisms leading to NIFs are still highly debated.

NIFs hold great potential as windows to Neoproterozoic ocean chemistry. They have relatively simple mineralogies dominated by authigenic mineral phases (Klein and Beukes 1993), making them useful geochemical archives because their mineralogical and isotopic properties speak to local and regional environmental conditions—and because the scavenging capacity of primary iron oxides can track ocean chemistry more broadly (e.g., Bjerrum and Canfield 2002; Konhauser et al. 2007; Konhauser et al. 2009).

Measuring major and trace element compositions, iron isotope properties, and rare earth element (REE) patterns adds constraints to the depositional model of NIFs. Iron isotopes (Johnson et al. 2008; Halverson et al. 2011) and REEs have the potential to indicate ocean redox conditions and iron sources for Banded Iron Formations (BIFs) (Klein and Ladeira 2004; Baldwin et al. 2011) and IFs (Derry and Jacobsen 1990).

The present study adds to the discussion a uniquely comprehensive sample set from the Neoproterozoic Fulu Formation of South China with the aim of revisiting the factors controlling its deposition as well as its regional and possibly global implications. The Fulu Formation was deposited as glaciers retreated within the Yangze Platform at the termination of the first global Neoproterozoic glaciation—the Sturtian—and is the youngest member of the Jiangkou Group, deposited between roughly 720–663 Ma (Zhang et al. 2011). We have used iron isotopes, rare earth elements, and trace and major element chemistry to identify a depositional environment in a restricted rift basin with an

ample supply of hydrothermal iron under partially reducing conditions—with the possibility of additional iron inputs via glacial sources.

The eventual demise of IFs near the end of the Neoproterozoic Era coincides generally with increasing, albeit still vacillating, oxygen levels in the ocean and presumably the atmosphere (Sahoo et al. 2012) and the emergence and diversification of animals—suggesting an important cause-and-effect relationship among dramatic climate change, biospheric redox, and the rise of complex life.

2. Background

2.1. Neoproterozoic Iron Formations

Between 717 and 635 Ma, the Neoproterozoic Era likely experienced at least two episodes of globally extensive glaciations (Hoffman et al. 1998; Hoffman and Schrag 2002; Rooney et al. 2014). Extensive continental ice cover and a suppressed hydrologic cycle may have limited riverine sulfate delivery to the ocean (Hurtgen et al. 2002), which would have enhanced iron availability in the anoxic deep ocean. Iron reaches the ocean through hydrothermal activity, continental weathering, dust deposition, and glacial debris, among other routes (Raiswell and Canfield 2012). Models of NIFs often provide evidence of a mixture of hydrothermal and detrital sources of ferrous iron (Cox et al. 2013); however, the relative influence of each can vary among sites.

IFs and specifically BIFs associated with the first and likely largest glaciation are found all over the world (Klein 2005; Cox et al. 2013) including the Rapitan IF in Canada (Young 1976), the Urucum IF in Brazil (Klein and Ladeira 2004), and the Chestnut Hill IF in the United States of America (Gates and Volkert 2004), to name a few. NIFs do not

share the distinct, well defined banding of Archean and Paleoproterozoic BIFs; instead, banding within NIFs tends to show poorly developed layers of hematite and chert (Cox et al. 2013). The fractions of iron existing as hematite can reach 50 weight percent, and organic carbon contents are typically insignificant (Hoffman et al. 2011). Accessory minerals occur primarily as mica, chlorite, and quartz. Some NIFs, including those in the Jacadigo Group in Brazil, contain high concentrations of manganese (Klein and Ladeira 2004), although most NIFs are predominantly composed of ferruginous laminated siltstone.

NIFs are largely associated both spatially and temporally with submarine mafic volcanoes (Bekker et al. 2010) and are found in basins within the supercontinent Rodinia as well as rift basins on its margins. NIFs can be linked to the continental rifting of Rodinia, which occurred between 830 and 740 Ma (Li et al. 2004), based on their thickness patterns and frequent associations with volcanic rocks (Yeo 1981). Furthermore, their REE signatures suggest deposition in restricted basins with local hydrothermal sources of iron (Derry and Jacobsen 1990); the universally high iron and silica contents of NIFs are consistent with a hydrothermal origin (Gurvich 2006) through the reaction of seawater with basalt-related sediment (Bischoff and Dickson 1975). It is also possible, however, that inputs of glacially sourced iron oxyhydroxides contributed to the elevated concentrations of iron within the Neoproterozoic Ocean (Baldwin et al. 2012), leading to uncertainties about the overarching source-sink relationships. The glaciers likely scoured the continents and held abundant iron-rich sediments (Swanson-

Hysell et al. 2010), which, in tandem with low sulfate and increased iron input, could have initiated and maintained a ferruginous Neoproterozoic ocean (Canfield et al. 2008).

Iron oxyhydroxides, the precursor to the iron oxides we find in NIFs, likely originated from an encounter between dissolved ferrous iron and a local, limited oxidant (Hoffman et al. 1998), or possibly through oxidation by anoxygenic photosynthesis (photoferrotrophy) (Konhauser et al. 2002). NIFs may have precipitated during the rapid retreat of globally distributed glaciers, as seawater newly exposed by melting sea ice encountered the oxygenated atmosphere (Kirschvink 1992, Klein and Beukes 1993, Hoffman et al 1998). They may also have deposited during the glaciation, as oxic subglacial meltwater met the underlying ferrous water (Hoffman 2005). In regions with thin glacial and sea ice cover, possibly just prior to melting, enough light may have been able to penetrate the ocean, enabling photoferrotrophy (Garrels et al. 1973; Hartmann 1984; Widdel et al. 1993; Konhauser et al. 2005), which would anaerobically oxidize ferrous iron by using Fe^{2+} as an electron donor in lieu of H_2O, producing ferric iron.

Growing evidence points to a deep ferruginous ocean of the Neoproterozoic Era (Canfield et al. 2008) with parallel indications of increased dissolved ferrous iron availability due to the relatively low levels of sulfate (Canfield et al. 2004) and often limited supplies of the organic matter required by bacteria to reduce sulfate to hydrogen sulfide, which can remove dissolved iron through pyrite formation. The strong depletion in sulfate during global glaciations allowed hydrothermal iron to build in concentration without risk of precipitation as FeS and FeS_2. The ocean's low sulfate content likely created a more iron-rich hydrothermal system, which greatly enhanced iron solubility in

the Neoproterozoic Ocean (Kump and Seyfried 2005), helping to pave the way for NIF deposition.

2.2. Geologic Setting.

Neoproterozoic formations from South China have much in common with those from eastern Australia and western Laurentia, leading to hypotheses of one large Neoproterozoic basin (Eisbacher 1985). According to the "missing-link" hypothesis, South China likely sat between Western Laurentia and Eastern Australia within Rodinia (Figure 1) (Li et al. 1995), because of incongruities between crusts of East Australia and Laurentia, similarities in the Neoproterozoic stratigraphy of South China, southeastern Australia, and western Laurentia (Eisbacher 1985), and resemblances between crusts of the Cathaysia Block of southeastern South China and southern Laurentia (Li et al. 2008).

Major rifting during the late mid-Proterozoic to early Neoproterozoic set the tectonic scene for deposition of Neoproterozoic IFs. Ultramafic volcanic rocks formed concurrent with the rifting, prior to IF deposition (Zhang et al. 2011). Volcanism, climate, and sedimentologic controls were conducive to the formation of IFs. The first global glaciation of the Neoproterozoic, often referred to as the Sturtian Glaciation, also carries the name Nanhua Glacial Epoch when in reference to glacial rocks of South China (Jiafu et al. 1987). The Fulu Formation likely deposited in the Nanhua Rift Basin, which was closely tied to mafic volcanism (Tang et al. 1987). The Fulu is underlain by pebble-bearing sandy slate and diamictite and was initially considered an interglacial deposit (Jiafu et al. 1987) until it was reassigned as a waning glacial deposit, with the overlying Datangpo Formation identified as the interglacial interval (Zhang 2003).

The Fulu Formation is part of the Sinian System on the Yangtze platform in South China (Figure 2). The passive margin on the Yangtze platform formed as it broke away from the supercontinent Rodinia.

Between around 1140 and 900 Ma, the Yangtze and Cathaysian plates collided along the southeastern margin of the Yangtze region (Li et al. 2008). The Nanhua rift began around 820 Ma at the marginal area of the plate (Wang and Li 2003). Between 830-795 Ma and 780-745 Ma, two instances of volcanic magmatic activity occurred (Li et al. 2003); the first started just before the rift, peaking immediately prior to the rift, and the second accompanied the main rifting stage. The Neoproterozoic strata were deposited within basinal facies in the southeast part of the Yangtze block following the breakup.

The Sinian System is made up of four unconformity-bounded sequences: the oldest contains the Baizhu and Hetong formations, the next consists of the Sanmenjie and Gongdong formations, the third is defined by the Chang'an and Fulu formations, and the youngest sequence comprises the Nantuo tillites and the Doushantuo and Dengying/Laobao formations of Ediacaran age (Wang et al. 2002). The Chang'an and Fulu formations are likely correlated with the Sturtian glaciation in Australia, as well as the last rift phase in southeastern Australia, which took place during the Sturtian period of glaciation (Preiss 2000). The Fulu formation corresponds to the waning cycle of the Sturtian glaciation, which likely occurred around 662.4 +/- 3.9 Ma, having lasted around 55 Ma (Rooney et al. 2014).

2.3. Iron isotopes

The magnitude of iron isotope fractionations due to redox changes eclipses all other fractionations associated with iron cycling (Johnson et al. 2008b). Iron enters the ocean in a variety of ways, but important to the Neoproterozoic Era are glacial and hydrothermal routes. Isotope fractionations track processes that control inputs and outputs of iron to the ocean, including biological cycling and associated redox changes and mineral speciation (Johnson et al. 2002).

Dissolved surficial ferrous iron is often oxidized by biologic and abiologic processes that result in ferric oxides, such as hematite, goethite, and magnetite, which often show enrichments in the heavier iron isotope (Johnson et al 2008a). Aqueous iron species or minerals that contain solely ferric iron have higher $\boldsymbol{\delta}^{56}$Fe values than those of mixed ferric and ferrous iron (Johnson et al. 2008b). For example, samples with hematite and magnetite that have high $\boldsymbol{\delta}^{56}$Fe values may have originated from reservoirs dominated by photosynthetic iron oxidation (Johnson et al. 2004), however, iron isotopes cannot readily distinguish between biotic and abiotic oxidative pathways because the fractionations for each are very similar (Anbar 2004).

Although $\boldsymbol{\delta}^{56}$Fe values cannot reveal oxidative pathways unambiguously, they can uncover differences in the amount of available oxidants relative to the supply of dissolved iron (Figure 3) (Li et al. 2013). Ferrous iron emanating from hydrothermal vents, as well as ferrous iron resulting from dissimilatory iron reduction (DIR), is characterized by near zero to negative $\boldsymbol{\delta}^{56}$Fe values, respectively. Upon oxidation, the resulting iron oxyhydroxides record a new $\boldsymbol{\delta}^{56}$Fe value reflecting the redox change and, often, the size of the dissolved iron reservoir. Under partially oxidizing conditions, the

resulting iron oxyhydroxides show high δ^{56}Fe values relative to the low δ^{56}Fe of the residual ferrous pool. The iron oxyhydroxides undergo dehydration to eventually bury as hematite while maintaining the large initial δ^{56}Fe value (Li et al. 2013). NIFs predominately record high δ^{56}Fe and δ^{57}Fe values, reaching δ^{57}Fe values of +1.2‰ in the Rapitan (Halverson et al. 2011), suggesting deposition under oxygen-limited conditions (partial oxidation) possibly in association with a comparatively large marine reservoir of dissolved iron (Halverson et al. 2011).

2.4. Rare earth elements

Rare earth elements (REEs) often play an important role in efforts to elucidate marine geochemistry. Specifically, relative concentrations between heavy (HREEs) and light (LREEs) provide ocean redox constraints (Goldstein and Jacobsen 1988), and europium and cerium can yield telltale anomalies, relative to average crustal sediments, under particular source and redox conditions (Elderfield and Greaves 1982). Positive europium anomalies reflect contributions from high-temperature hydrothermal fluids (Bau and Dulski 1999), and negative cerium anomalies reflect oxidized marine waters (German and Elderfield 1990).

Archean IFs are enriched in Eu relative to the other REEs, which means Eu existed as Eu^{2+} in addition to Eu^{3+}; modern seawater lacks this Eu enrichment (Fryer 1976) because under oxic conditions, hydrothermal vent fluids are a sink for seawater REEs due to their co-precipitation with Fe oxides (Kamber and Webb 2001). During the Neoproterozoic, scavenging of divalent Eu from hydrothermal fluids onto iron oxyhydroxides was likely a major control on limiting the large Eu flux from

hydrothermal vents to the ocean (Derry and Jacobsen 1990). The reducing state of hydrothermal solutions (Bowers et al. 1985) and the stability fields of Eu species (Sverjensky 1984) indicate that divalent Eu is the stable form of Eu in reducing hydrothermal fluids until Eu encounters and is heavily diluted by ambient seawater. Once Eu is oxidized to Eu^{3+}, it behaves similarly to other REEs (Bryne et al. 1988). Marine REE patterns without a prominent Eu anomaly also reflect inputs of dissolved and detrital REEs from riverine sources originating from the continents (Elderfield 1988).

Negative Ce anomalies reflect oxic seawater; when oxidized, less soluble Ce^{4+} is preferentially scavenged by Mn particles, crusts, and nodules (Piper 1974; Elderfield et al. 1981) and Fe-Mn oxides coating sediment particles, leaving a relative Ce deficiency in the seawater host. By contrast, suboxic and anoxic waters do not contain noteworthy negative Ce anomalies because of reductive dissolution of settling Mn-Fe-rich sediments and can even show positive anomalies marking the preferential transport and release of Ce from oxic to anoxic waters (German et al. 1991; Byrne and Sholkovitz 1996; Planavsky et al. 2010).

The modern ocean contains REE patterns that are noticeably HREE enriched, consistent with the prevailing oxic conditions; light REEs attach preferentially to Mn-Fe oxyhydroxides and other reactive surfaces because of differences in REE particle reactivity (Elderfield and Greaves 1982). Overall REE patterns remain fairly constant throughout time, with the exception of HREE or LREE enrichment as well as europium and cerium anomalies.

Hydrothermal plumes often contain an enrichment of up to 1000 times the REE concentrations of seawater (Michard et al. 1983). REEs within hydrothermal plumes experience removal processes such as scavenging and co-precipitation onto iron oxides (Klinkhammer et al. 1983). As the hydrothermal plumes rise above their venting site they are diluted by the surrounding seawater by a factor of roughly 10,000 and then further diluted as the plume spreads laterally (Mitra and Elderfield 1994). Iron oxyhydroxides co-precipitate and scavenge hydrothermally derived REEs; resulting REE patterns show enrichment in the light REEs and a large positive Eu anomaly (Mitra and Elderfield 1994).

The fate of hydrothermally emitted REEs is dependent on the amount of jointly released hydrothermal iron. REE/Fe ratios can indicate various scenarios: the vent fluid REE/Fe can be equal to that of the iron oxide precipitate, the vent fluid ratio can be greater than the iron oxide REE/Fe, and finally the vent fluid REE/Fe can be less than the sediment ratio (Olivarez and Owen 1989). These relationships will guide our use of REE to illuminate conditions of, and controls on, NIF production in South China—as particularly related to overarching Fe availability and the relative magnitude of hydrothermal inputs.

When the vent fluid ratio is equal to the iron oxide ratio, it is probable that iron oxide precipitates are co-precipitating or scavenging REEs quantitatively. If precipitates remove all the REEs, surrounding seawater remains unaffected. Under conditions in which the vent fluid REE/Fe is greater than the precipitate REE/Fe, some of the REEs were able to escape iron oxide scavenging, or the iron content was low enough to limit

potential REE removal (Olivarez and Owen 1989). The REEs that emit from hydrothermal vent sites often do not affect overall REE concentrations within marine waters because the REEs are entirely scavenged by the iron oxyhydroxides at the site of venting (Ruhlin and Owen 1986; Olivarez and Owen 1989), especially during the Neoproterozic Era, which likely saw exceptionally high iron contents in hydrothermal vents (Kump and Seyfried 2005).

3. Methods and Materials

3.1. Samples

We obtained Neoproterozoic IF and BIF samples from the South China Fulu Formation. We visited three outcrop localities: the Mengzhai and Fengmu sections in Sanjiang County, Guangxi Province, and the Jiangkou section in Dongkou County, Hunan Province. Samples from Jiangkou, Fengmu, and the Mengzhai sections are denoted as SCF (South China Fulu), SCF – 2, SCF – 3, respectively.

Samples were cut on a diamond saw to remove weathered surfaces. The homogenous and banded samples were powdered in a ceramic ball mill. A Dremel rotary tool with a diamond tip was used to target and powder individual bands.

3.2. Mineralogical analysis

X-Ray Diffraction (XRD) was performed at Rensselaer Polytechnic Institute with a Bruker D8-Discover diffractometer. Powdered samples were loaded onto disks and analyzed with a Cu sealed-tube X-ray source. Every sample, as well as individual bands within certain samples, underwent XRD analysis.

A Nova NanoSEM450 Schottky Field Emission Scanning Electron Microscope (SEM) at University of California, Riverside, was used to obtain detailed mineralogical images and compositions. The SEM combines high and low voltage ultra-high resolution capabilities with low-vacuum, high resolution imaging systems. Integrated Energy Dispersive X-ray Microanalysis (EDS) and an Electron Backscattered Diffraction system (EBSD) from Oxford Instruments provided qualitative and quantitative chemical analysis and image capture. The EBSD used X-ray spectral mapping to identify mineral phases and map elemental distributions. Sections were prepared for seven samples, including at least one from each of the three outcrops, and were analyzed on the SEM.

3.3. Total acid digests

100-200 mg of sample powder was combusted in a muffle furnace at 550°C for 8-12 hours. The ashed sample was then transferred to a 15 ml Teflon vessel along with 5 ml of concentrated nitric acid and 1 ml of concentrated hydrofluoric acid. Samples were sonicated and then heated inside a dry-down box at 120 C for at 8 – 12 hours. After the powders dissolved, the Teflon vessels were uncapped, which allowed the solution to evaporate, leaving a damp sample residue behind. Aqua Regia was then added to the Teflon vessels at a ratio of 1 ml of HNO_3 to 3 ml of HCl. Samples were sonicated and then heated for 8 – 12 hours. When undigested particles remained after the initial Aqua Regia addition, the entire Aqua Regia process was repeated. Once the powders were completely digested, the samples were brought up to approximately 5 ml with 2% HNO_3. The resulting solutions were analyzed on an Agilent 7500ce ICP-MS at University of California, Riverside, to determine elemental data.

3.4. Iron isotope analyses

Processing of digested samples was undertaken in a clean laboratory at the Laboratory of Geochemistry and Cosmochemistry, Institut de Physique du Globe de Paris. The digested powders, in 2% trace metal grade nitric acid, were transferred to Teflon beakers and evaporated to dryness. They were twice acidified with mixtures of HCl-HNO_3 and evaporated to ensure that all Fe was in the ferric state before loading on the resin. All samples were then dissolved in 6 M HCl before the ion exchange chromatography. The following ion chromatography procedure was performed twice for each sample to ensure separation of Fe from matrix elements. Bio-Rad Poly-Prep columns were filled with 1 mL anion exchange resin (AG1-X8 200-400 mesh chloride form). The resin was cleaned three times with 10 ml H_2O and 5 ml 1 M HNO_3. It was then preconditioned in HCl medium by running 10 ml H_2O, 10 ml 0.4 M HCl, 5 ml H_2O and 2 ml 6 M HCl. Half of the sample solution (250 ml) was loaded on the column in 6 M HCl (containing between 10 and 500 mg of Fe). Matrix elements were eluted with 8 ml 6 M HCl, whereas Fe(III) is strongly adsorbed on the resin and is quantitatively retained. Fe was subsequently eluted in 10 ml 0.4 M HCl, with a procedural yield of >94%. The Fe blank level of the present procedure has been evaluated by systematic analyses of one blank in each sample series, prepared as described above but without any sample powder or solution. The blank was always below 40 ng Fe (average ~30 ng), thus representing less than 0.4 % of the bulk Fe.

Iron concentrations and isotopic compositions were measured using a Neptune ThermoFischer MC-ICP-MS (Multiple Collector Inductively Coupled Plasma Mass

Spectrometer) at the Laboratory of Geochemistry and Cosmochemistry. Isotopic ratios are expressed using the standard δ notation: $\delta^{56}Fe = (^{56}Fe/^{54}Fe_{Sample}/^{56}Fe/^{54}Fe_{Standard} - 1)*1000$, expressed in per mil (‰) and relative to the IRMM-014 standard, also referred to as IFG (Anbar 2004)

3.5. Rare earth element analyses

Analyses of REEs were carried out at Yale University on a ThermoElectron Inc. Element2 inductively coupled plasma mass spectrometer (ICP-MS). Digested solutions in 2% trace-metal grade nitric acid were introduced to the plasma via a Cetac Apex desolvating nebulizer to minimize isobaric interferences, such as $135Ba16O^{+}$ on $151Eu^{+}$. Ba and Ce spikes were aspirated periodically to monitor the formation of Ba and REE-oxides. Ba-oxide formation was insignificant. REE-oxides constituted less than 4% of the total REE concentration. 5 ppb of internal standard were added to each sample to correct for fluctuations of the plasma during analysis. For REE, we used Specpure plasma solution standards, and background intensities were measured by aspirating 5% HNO3 blanks.

Accuracy of the analysis is conservatively around 10%, and the REE ratios are likely accurate within 10% based on standard and sample duplicates throughout the analytical run. REE data were normalized using Mud from University of Queensland (MuQ), which is a shale composite, because it contains an upper-continental crust value unaffected by diagenesis.

4. Results and Discussion

4.1. Mineral Compositions

Geochemical studies of IFs often emphasize whole-rock approaches, which include both iron and chert bands in a single sample. For this study, however, we found it useful to separate the bands for analysis of solution chemistry and mineralogies to better understand the conditions that gave rise to these unique sediments. We used XRD and SEM, applied to individual bands, to explore mineralogical relationships in detail.

We identified hematite ($Fe^{3+}_2O_3$) as the primary iron oxide mineral and quartz (SiO_2) as the primary chert layer component throughout all the samples based on XRD analysis. Hematite has been recognized previously as the predominant iron oxide in NIFs (Klein and Beukes 1993). Although magnetite ($Fe^{2+}_2Fe^{3+}O_4$) was not identified as a primary mineral in any of the samples, it is likely it to be present in small amounts in samples of the Jiangkou section, which reacted slightly to a magnet. Magnetite has not been reported as the primary iron-bearing phase in NIFs except in metamorphosed deposits (Cox et al. 2013). For example, minor magnetite has been identified in the Neoproterozoic Chestnut Hill Formation (Gates and Volkert 2004), the Arabian-Nubian Shield (Ali et al. 2009; Basta et al. 2011), and the Braemar iron formation in South Australia (Lottermoser and Ashley 2000). These low occurrences of magnetite in NIFs indicate that they have not encountered much metamorphism.

EBSD analyses on the SEM identified hematite as the dominant iron-bearing mineral in each sample analyzed, supporting the XRD analyses. EBSD analyses also provided detailed mineralogical maps from which we could identify specific accessory minerals such as mica, biotite, albite, and chlorite, which may indicate that the Fulu

formation incorporated minor amounts of metamorphosed minerals that may have formed during the rifting of Rodinia, just prior to the Fulu's deposition.

We processed a representative set of samples, including at least one from each of the three outcrop localities through SEM EBSD analyses to map their mineralogical makeup. Among the broadly representative samples chosen, SCF 2-21 contains an iron oxide-dominated band alongside a thicker, relatively iron-depleted chert band (Figure 4A). Accessory minerals can be identified by the gray levels in Figure 4B; they are mostly mica, biotite, and chlorite in this sample. The iron-poor layer is almost exclusively quartz and contains chlorite and biotite as accessory minerals. The bright spots in the SEM picture in Figure 4B highlight the iron oxide (hematite) minerals; the darkest gray represents quartz grains, and the varying lighter grays depict the accessory minerals, such as mica, chlorite, and biotite. The thin section in Figures 4A shows generally poor banding with darker iron-oxide bands alternating with lighter sandy or silty chert bands.

4.2. Jiangkou Formation

The Jiangkou section is from the base of the Fulu Formation directly overlying the glacial, diamictite-abundant Chang'an deposits. The section is specifically located at 27°11'36 N, 110°24'51 E and is predominately massive with some rare chert nodules and beds of diamictite, indicating an interstadial environment. The stratigraphic column of the Jiangkou (Figure 5A) shows mostly fine-grained siltstone and sandy shale, along with massive ironstones. The collected samples were mostly homogenous in composition. None of the Jiangkou samples showed banding, although some sand samples contained clasts of glacially delivered lonestones. The Jiangkou's deep water setting likely

prevented the banding we see in the shallower Fengmu and Mengzhai sections, which took advantage of variations in the availability of oxygen (Cloud 1973) and light (Konhauser et al. 2007) as the glaciers retreated at the surface of the ocean.

Redox is the strongest control over the behavior of iron in terms of its isotopic and mineralogical properties. Iron is soluble in reducing environments as Fe^{2+}; reactions with oxygen cause iron to precipitate out of solution in its Fe^{3+} form either as an iron oxyhydroxide or iron oxide.

Fe_T/Al ratios can reveal iron enrichments that strongly suggest iron-rich anoxic depositional conditions, and these enrichment patterns can be assessed against a baseline of detrital/continental sources that are often remarkably consistent in terms of their bulk Fe properties, with Fe_T/Al ratios close to 0.5±0.1 (Lyons et al. 2003; Lyons and Severmann, 2006; Raiswell et al., 2008). High Fe_T/Al ratios seen throughout the samples argue for syngenetic or authigenic enrichment in the water column or sediments, respectively. For example, high Fe_T/Al ratios for the Jiangkou section, often about two times the values for continental sources, (Figure 5C), when combined with low degrees of pyritization, are diagnostic of ferruginous (iron-rich, sulfide-poor) depositional conditions (Lyons and Severmann 2006). In the presence of dissolved sulfides, iron will precipitate as pyrite or its 'FeS' precursors. Figure 5B shows relatively low Mn contents, from 0.03 to 0.10 weight percent, higher Al concentrations, ranging from 2 to 5 weight percent, and high iron contents, from 3 to 24 weight percent.

The high $\delta^{56}Fe$ values (Figure 5D) point to relatively oxygen-limited conditions in predomininately ferruginous waters with an ample source of iron (discussed in more

detail in Synthesis section). More specifically, the large inferred fractionations in the oxide phases are consistent with partial Fe oxidation, and the positive relationship between Fe_T/Al and $\delta^{56}Fe$ values (Figure 8B) points to a direct relationship between reservoir size and resulting fractionations. Higher $\delta^{56}Fe$ values presumably resulted from an ample pool of iron. We suggest that hydrothermal plumes, with minor input from glacially delivered iron, likely emitted abundant reduced iron-rich fluids that interacted with minimal oxygen to form iron oxyhydroxides with high $\delta^{56}Fe$ values. Variations in $\delta^{56}Fe$ values were small, indicating similar iron sources throughout the section and the likelihood of a persistently abundant Fe reservoir. The positive correlation between Ti and Al points to inputs of detrital sediments decoupled from the possible hydrothermal contributions. The high Fe/Al and Fe/Ti ratios are consistent with a hydrothermal source for iron against a background of detrital sedimentation (Bostrom et al. 1969).

All the samples from the Jiangkou contain positive shale-normalized (SN) Eu anomalies (Eu/Eu*), calculated as $Eu_{(SN)}/0.66Sm_{(SN)}+0.33Tb_{(SN)}$, which considers the slight positive seawater Gd anomaly (Planavsky et al. 2010). The Jiangkou section lacks the cross-stratification and ripple marks of the shallow Fengmu and Mengzhai sections, and shows distinct positive Eu anomalies, ranging from 2.52 to 4.17 (Figure 5E and 9A), suggesting deposition in a deeper setting with a proximal hydrothermal source.

The Jiangkou samples lacked any significant shale-normalized Ce anomaly ($Ce/Ce_{(SN)}$ *) (Figures 8A and 9A), measured as ($Ce_{(SN)}/0.5Pr_{(SN)} + 0.5\ La_{(SN)}$). Pr anomalies (Pr/Pr*), calculated by ($Pr_{(SN)}/(0.5Ce_{(SN)} + 0.5Nd_{(SN)})$) work with $Ce/Ce_{(SN)}$ * to differentiate between positive La and true negative Ce anomalies (Figure 8A) (Bau and

Dulski 1996; Planavsky et al. 2010). A lack of negative Ce anomalies provide further evidence for minimal oxygen concentrations during NIF genesis, consistent with our argument for partial Fe oxidation yielding large Fe isotope fractionations and thus relatively heavy δ^{56}Fe values.

4.3. Fengmu Formation

The Fengmu section is located between the Jiangkou and Mengzhai sections at 25°57'29 N, 109°38'17 E and contains abundant sandstone that is dominated by sand grains, fine grain sizes, and quartz grains with clasts of lonestones. We observed well-defined BIFs, massive facies, and siderite-rich sands (Figure 6A). Hematite is prevalent throughout the section with shale layers that reflect the detrital sediment inputs delivered via wind or rivers. The section is underlain by over 100 m of sand, the upper 100 m of which contains intervals of lamination.

The Fe_T/Al content (Figure 6C) is high, as are the δ^{56}Fe values (Figure 6D), which indicate abundant iron availability in an oxygen-limited environment. Similarly, the positive relationship between δ^{56}Fe and Fe_T/Al reveals reducing conditions with high iron contents. Here too we suspect hydrothermal sourcing into an anoxic environment. Figure 6B depicts variations in weight percents of Mn (black squares), ranging from 0.01 to 0.14 wt%, Al (grey circles), incuding values from 2.10 to 5.68 wt%, and Fe (black triangles), which range from 1.75 to 38.89 wt%.

4.4. Mengzhai Formation

The Mengzhai section is the shallowest deposit—located at 25°52'01 N, 109°27'39E. The Mengzhai contains a thin, ooid- and calcite-rich carbonate base about

1meter thick; very fine sand separates the two main intervals of sample collection. Banding was prevalent in most of the iron-rich samples, and detrital grains were extremely fine, bordering on mud-sized (Figure 7A). The samples are very hematite-rich; the iron-rich bands contained showed the highest Fe_T/Al ratios and highest $\delta^{56}Fe$ values relative to the Jiangkou and Fengmu sections (Figures 6C and D). Samples from the carbonate base yielded very low $\delta^{56}Fe$ values, which is typical for carbonates, reflecting low amounts of detrital Fe (Johnson et al. 2008a). Iron oxide samples towards the top of the Mengzhai section showed a positive correlation between $\delta^{56}Fe$ and Fe_T/Al (Figure 8D)—consistent with the notion of relatively large expressed Fe fractionations under Fe-replete conditions versus lower net fractionations when Fe is more limiting. Figure 7B depicts weight percents of Mn (black squares), which ranges from 3.06 to 54.00 wt%, Al (gray circles), including values 0.07 to 5.74 wt%, and Fe, which ranges from 0.01 to 0.30 wt%.

The REE distribution for the Mengzhai section lacked both a positive Eu anomaly and a negative Ce anomaly (Figure 7E and 9 B), possibly suggesting glacial sourcing of reduced iron oxyhydroxides. However, input from glaciers was likely overwhelmed by input from hydrothermal fluids that experienced significant seawater dilution and/or the possibility of high REE/Fe vent fluids that emplaced under predominately reducing conditions. The positive relationship between Ti and Al point to detrital inputs; the high Fe/Al and Fe/Ti values point to a hydrothermal source of iron that encountered and incorporated relatively minor amounts of detrital material.

5. Synthesis

5.1. Iron Isotopes

NIF deposition requires an iron source capable of providing abundant iron; glacial sources and hydrothermal vents are often implicated because each can provide large amounts of reduced iron. During dissimilatory iron reduction (DIR) of glacially delivered Fe(III) from iron oxyhydroxides, microbes use organic carbon as an electron donor to reduce Fe(III), releasing Fe(II) with δ^{56}Fe values up to 3‰ lower than the initial Fe(III) (Crosby et al. 2005; Berquist and Boyle 2006). The low δ^{56}Fe value of DIR-derived ferrous iron often translates to lower δ^{56}Fe values in resulting iron oxides (Johnson et al. 2008) (Figure 3).

Hydrothermally delivered iron contains δ^{56}Fe values close to 0‰, perhaps around -0.23‰ (Severmann et al. 2004); however, upon oxidation, Fe(III) shows a strongly positive δ^{56}Fe value via instantaneous fractionation, with net fractionation also reflecting the reservoir properties (Figure 3). Isotopic fractionation between the initial Fe^{2+} and the resulting ferric oxide/hydroxide can be around +1.5‰ at room temperature (Johnson et al. 2008). The oxidation pathway does not define the magnitude of fractionation, since anaerobic photosynthetic Fe^{2+} oxidation (Croal et al. 2004), acidophilic iron-oxidizing bacteria mediated oxidation (Balci et al. 2006), and UV-photo oxidation (Staton et al. 2006) do not differ significantly in their resulting δ^{56}Fe values. In the absence of reservoir effects, ferric oxide/hydroxides show the maximum fractionation and have δ^{56}Fe values that are roughly 1.5‰ greater than those of the initial Fe^{2+}.

For the IFs of the Fulu formation, which deposited during the waning period of the Sturtian glaciation, it is possible that bacterially reduced dissolved Fe(II) oxidized to Fe(III) once the ice withdrew (Baldwin et al. 2011) or the fluids were otherwise exposed to oxygen or light. However, influence from DIR was likely overwhelmed by input from hydrothermal vents due to the lack of organic matter (Halverson et al. 2011) and exceptionally high δ^{56}Fe values in the Fulu Formation—as further supported by our REE data at the Jiangkou section.

The observed variations in δ^{56}Fe values (Figures 5D, 6D, and 7D) throughout the sections correlate to banding and mineralogies; the iron oxide bands contained higher $\boldsymbol{\delta}^{56}$Fe values than their chert-rich neighbors. δ^{56}Fe values throughout the sections were high, indicating a similar source of iron with persistently low oxygen and high Fe availability. δ^{56}Fe variations that track inferred water depths were not as pronounced as variations in Fe_T/Al ratios: however, there was a positive relationship between the total concentration of iron and the δ^{56}Fe value.

δ^{56}Fe values were obtained for a variety of samples, including individual bands within BIFs. Trends in the Fengmu section among similar bands, i.e. iron-rich layers (Figure 6D), showed a slight decrease in δ^{56}Fe moving up the section, similar to trends seen in the Rapitan formation (Halverson et al. 2011), likely influenced by slightly more abundant available oxidants approaching the ocean's surface. The shallower sections likely encountered higher contents of oxygen and more direct exposure to light as their icy cover began to retreat. Our δ^{56}Fe values concentrated in the positive range, with a few exceptions in the Mengzhai section between -0.13‰ and -0.05‰—predominately in

samples containing carbonate. Values for $\delta^{56}Fe$ were generally high, with extremes among the iron-rich bands of Mengzhai section BIFs that reach +1.80‰, also seen in previous research on the Fulu (Bin et al. 2010). The very large $\delta^{56}Fe$ values of the Mengzhai and Fengmu sections are found within the iron oxide bands of BIFs. The iron-rich bands contain the highest Fe_T/Al values of all samples throughout the three sections; it is possible that these iron oxide bands record periods of intense ferrous iron buildup during deposition of chert layers, culminating in rapid oxidation as an iron oxide with minimal available oxygen.

Magnetite may have slightly lowered $\delta^{56}Fe$ values for the Jiankou section within some samples. Although the deeper Jiangkou setting likely encountered very low oxygen contents, hematite is isotopically heavier than co-existing magnetite by 0.1–0.4‰ in $\delta^{56}Fe$ within individual samples (Li et al. 2013). Positive correlations between Fe_T/Al and $\delta^{56}Fe$ (Figures 8B and D) imply a positive relationship between high iron concentrations and low oxygen potentials.

Iron formations should capture the $\delta^{56}Fe$ values of the initial dissolved iron source when oxidation is complete (Planavsky et al. 2011), as we see near the Rainbow hydrothermal vent along the Mid-Atlantic Ridge (Severmann et al. 2004). In contrast, partial oxidation when Fe^{2+} supplies exceed oxygen availability results in large net fractionations. Specifically, partial microbial and abiotic Fe^{2+} oxidation produces Fe^{3+} oxides dominated by heavy iron isotopes, and IFs with heavy isotopic signatures likely reflect abundant hydrothermal iron delivery to sulfur-depleted, oxygen-limited oceans (Rouxel et al. 2005).

5.2. Rare Earth Element Patterns

The REE profiles for the Jiangkou (Figure 9A) and Mengzhai (Figure 9B) are remarkably different. The prominent positive Eu anomaly in the Jiangkou section is absent in the Mengzhai section, although both sections do not show negative Ce anomalies. Their shared lack of negative Ce anomalies and their enrichment in lighter REEs indicate that they deposited under conditions with minimal oxygen, also evidenced by the positive $\delta^{56}Fe$ values throughout all the sections and the implicit partial oxidation of dissolved Fe. Their very different Eu patterns illuminate the different paths the iron oxyhydroxide particles, the intermediate species between dissolved ferrous iron and final iron oxides, may have taken upon precipitation from a hydrothermal vent.

High iron concentrations were favored in the Neoproterozoic ocean as a result of the very minor sulfate content, which elevated the Fe/S_2 in hydrothermal vents (Kump and Seyfried 2005). Just prior to the deposition of the Fulu Formation, Rodinia broke up, supplying the ocean with abundant hydrothermally derived iron (Tang et al. 1987). The hydrothermally sourced iron may have far out-supplied its co-emitted REEs, leading to significantly lower vent fluid REE/Fe ratios. Once the entire input of hydrothermal REEs co-precipitated with the iron oxides or was scavenged by iron oxides, depositing as the Jiangkou section, excess iron was able to travel further and precipitate in the presence of seawater-sourced REEs (Olivarez and Owen 1989), leaving the Mengzhai section with a seawater-like REE profile.

If the REE/Fe ratio of hydrothermal vent fluids were closer to 1, it would indicate that all iron oxyhydroxides precipitated with or scavenged REEs close to the vent. The

Jiangkou section deposited in a deep-water setting distant and likely somewhat isolated from the Fengmu and Mengzhai sections. The prominent Eu anomaly carried by the samples within the Jiangkou section indicates that hydrothermal iron likely co-precipitated with and quickly scavenged REEs from hydrothermal fluids, travelling only a short distance through oxygen-depleted water—resulting in retention of the reduced, divalent form of Eu and a record of positive Eu anomalies. Eu anomaly values become more seawater-like with increasing distance from the source (Isley 1995), and so the strong diluting capabilities of seawater may fingerprint the distance traveled from plume prior to deposition. By this argument, the Mengzhai section strata was deposited further from the vent than the Jiangkou section and lost its positive Eu anomaly through seawater dilution. Positive Eu anomalies have also been identified in the Seridó Belt in Northeast Brazil and explained by close proximity to hydrothermal vents in anoxic deep waters (Sial et al. 2014).

The high Fe/S_2 ratio of hydrothermal fluids (Kump and Seyfried 2005) lends support to the notion of a lower vent fluid REE/Fe ratio. The proximal precipitates may have been able to scavenge all vent-sourced REEs efficiently, with the result that the Jiangkuo samples captured hydrothermally derived REEs and deposited in a deeper setting within a short distance from the vent source—yielding a positive Eu anomaly. The Mengzhai samples, by contrast, bear the signature of hydrothermal Fe but seawater REE and thus lack a positive Eu anomaly.

Research implicating glacially delivered iron as the primary iron source for the Neoproterozoic Rapitan formation cites a nonexistent positive Eu anomaly and

consequent ocean oxygenation to eliminate possible hydrothermal vent fluid inputs (Baldwin et al. 2012). However, this research fails to identify a negative Ce anomaly, which would diagnose oxygenation (Baldwin et al. 2012), or explain observed high $\delta^{56}Fe$ values, which point to oxygen limitation. The Rapitan formation's lacking Eu anomaly has been attributed to low temperature hydrothermal fluids, which provide ample ferrous iron without a positive Eu imprint (Halverson et al. 2011).

6. Future Work

The Jiangkou and Mengzhai sections deposits geographically bookend the Fengmu section REE analyses are needed for this section to better understand the REE signatures and their relationships to hydrothermal Fe sourcing. For example, we might expect intermediate signals given the sections geographic position between the other two. If the Fengmu section show a slightly diluted Eu anomaly, less than that of the Mengzhai section, it is likely that seawater dilution played a significant role in determining REE patterns. However, if the Fengmu lacks any Eu anomaly, similar to the Mengzhai, the vent fluids would have been exceptionally high in iron relative to REEs and thus able to supply two of the sections with iron lacking a hydrothermal REE imprint with possible glacial influences.

7. Conclusion

The Fulu Formation deposited post Rodinia rifting. The rifting phase likely led to an increase in the iron flux to the ocean that eventually became iron formations. In addition to the rifting, low riverine sulfate delivery to the ocean resulting from the global glaciations (Hurtgen et al. 2002), as well as low sulfur availability due removal from the

surface reservoir via subduction of sedimentary sulfides (Canfield 2004), led to reduced sulfate levels in the Neoproterozoic and favored redox conditions of midocean ridges hydrothermal systems that produced vent fluids with very high iron concentrations (Kump and Seyfried 2005).

Mantle plume events can also stimulate BIF deposition by elevating the iron flux into the ocean through submarine hydrothermal processes as well as favor the formation of intracratonic rift basins for deposition (Isley and Abott 1999). The glacially induced challenge to continental weathering placed a higher importance on hydrothermal sources of iron, with relatively minor input from glacially sourced iron oxyhydroxides that underwent dissimilatory iron reduction (Baldwin et al. 2012).

Hydrothermal iron likely sourced the vast majority of iron that made up the Fulu Formation, with the Jiangkou section bearing the telltale fingerprint of hydrothermally emitted REEs. The Mengzhai, in its more distal setting, possibly encountered seawater dilution or domination by seawater REEs that lacked a Eu anomaly. Exceptionally iron-rich hydrothermal vent fluids would have very low REE/Fe ratios, conducive to forming a deeper proximal Jaingkou section with a hydrothermal REE pattern and a more distal Mengzhai section with a seawater REE pattern.

Positive iron isotope signatures throughout the NIFs indicate a partially reducing environment that was gradually exposed to increasing amounts of oxygen and sunlight as overlying ice cover waned. Neoproterozoic Iron Formations mark the end of voluminous, widespread iron formations and hint at the rise of atmospheric oxygen, ocean ventilation, and the emergence and diversification of animals that followed—albeit still under very

dynamic redox conditions (Sahoo et al. 2012). Understanding the depositional controls on NIFs is a crucial step towards illuminating the precise relationships among the final appearance of iron formations, related tectonic controls, and the ultimate rise in atmospheric oxygen and proliferation of complex life.

Figures

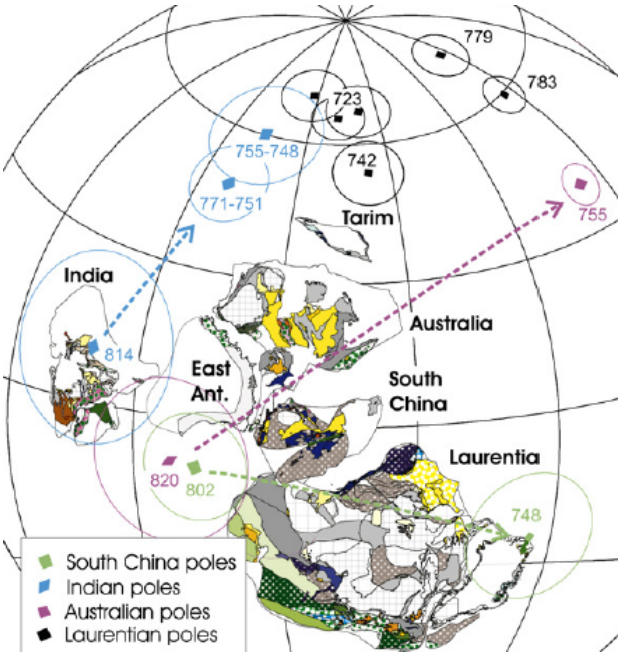

Figure 1. Possible reconstruction of the supercontinent Rodinia; “Missing-Link” model, which places South China (the “missing-link”) between East Australia and Laurentia within Rodinia. From Li et al. (2008)

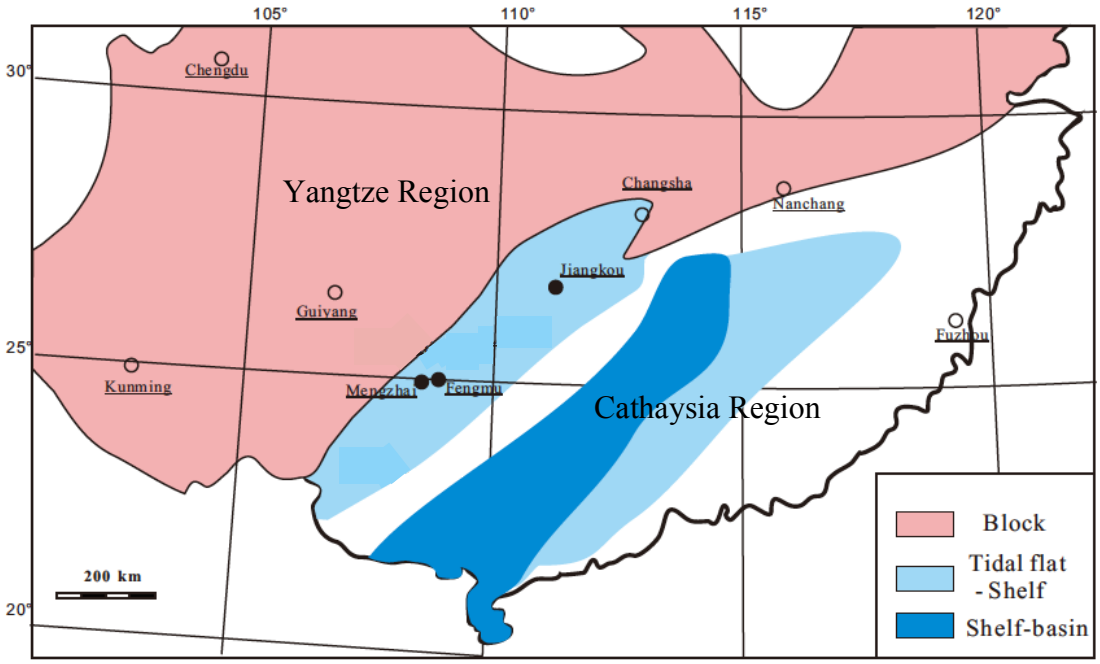

Figure 2. The South China Block, which contains the Yangtze and Cathaysia blocks. Outcrop localities are marked by filled in circles as Jiangkou, Fengmu, and Mengzhai. Empty circles identify surrounding cities. Modified from Wang and Li 2003.

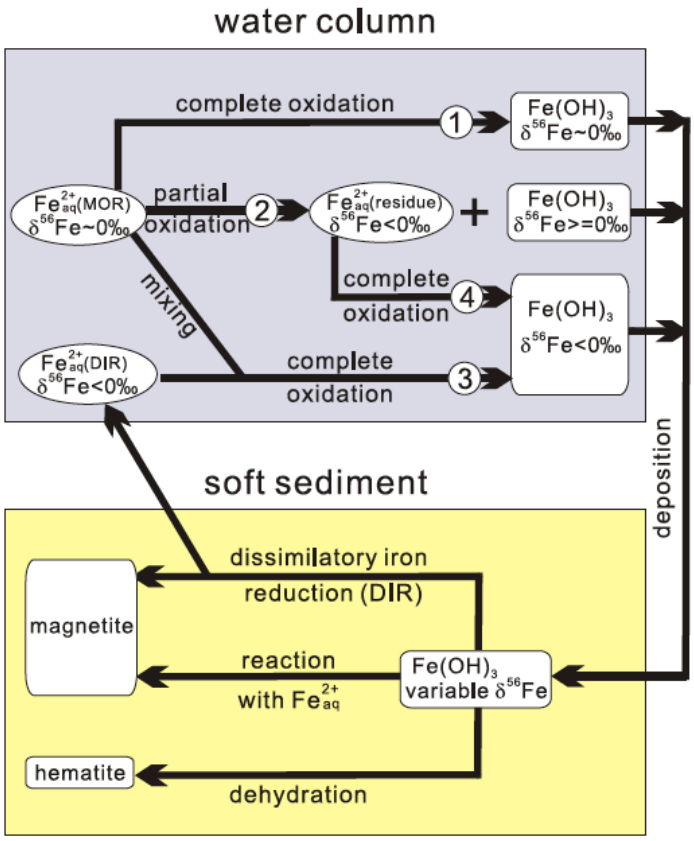

Figure 3. Hydrothermal iron emitted from a mid-ocean ridge $Fe^{2+}_{aq(MOR)}$ undergoes complete oxidation, partial oxidation, and mixing with $Fe^{2+}_{aq(DIR)}$, which is reduced iron derived from dissimilatory iron reduction. $Fe^{2+}_{aq(MOR)}$ undergoing partial oxidation produces a depleted $\boldsymbol{\delta}^{56}$Fe for residual reduced iron, and a positive $\boldsymbol{\delta}^{56}$Fe for iron oxyhydroxide. The resulting positive $\boldsymbol{\delta}^{56}$Fe iron oxyhydroxide can then undergo dehydration to form hematite. From Li et al. (2013).

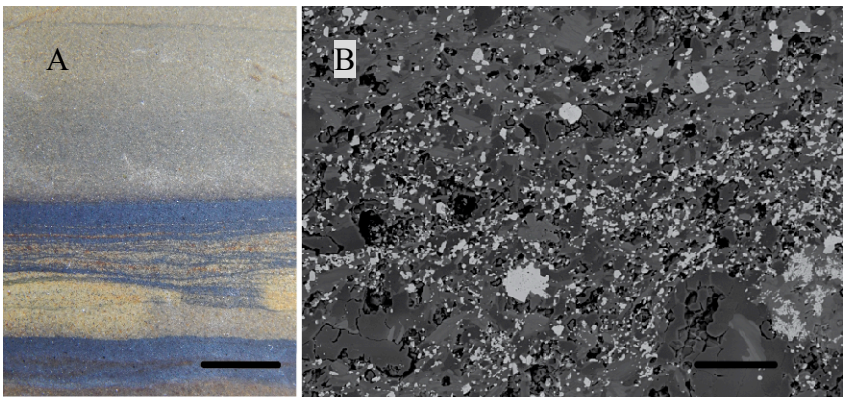

Figure 4. Thin section and SEM EBSD images from the Fengmu section (A) Sample SCF 2-21, bar is 5mm. (B) Sample SCF 2-21, bar is 50 nm. (B) provides a detailed mineralogical look at a typical iron-rich layer, represented by the dark lines in (A).

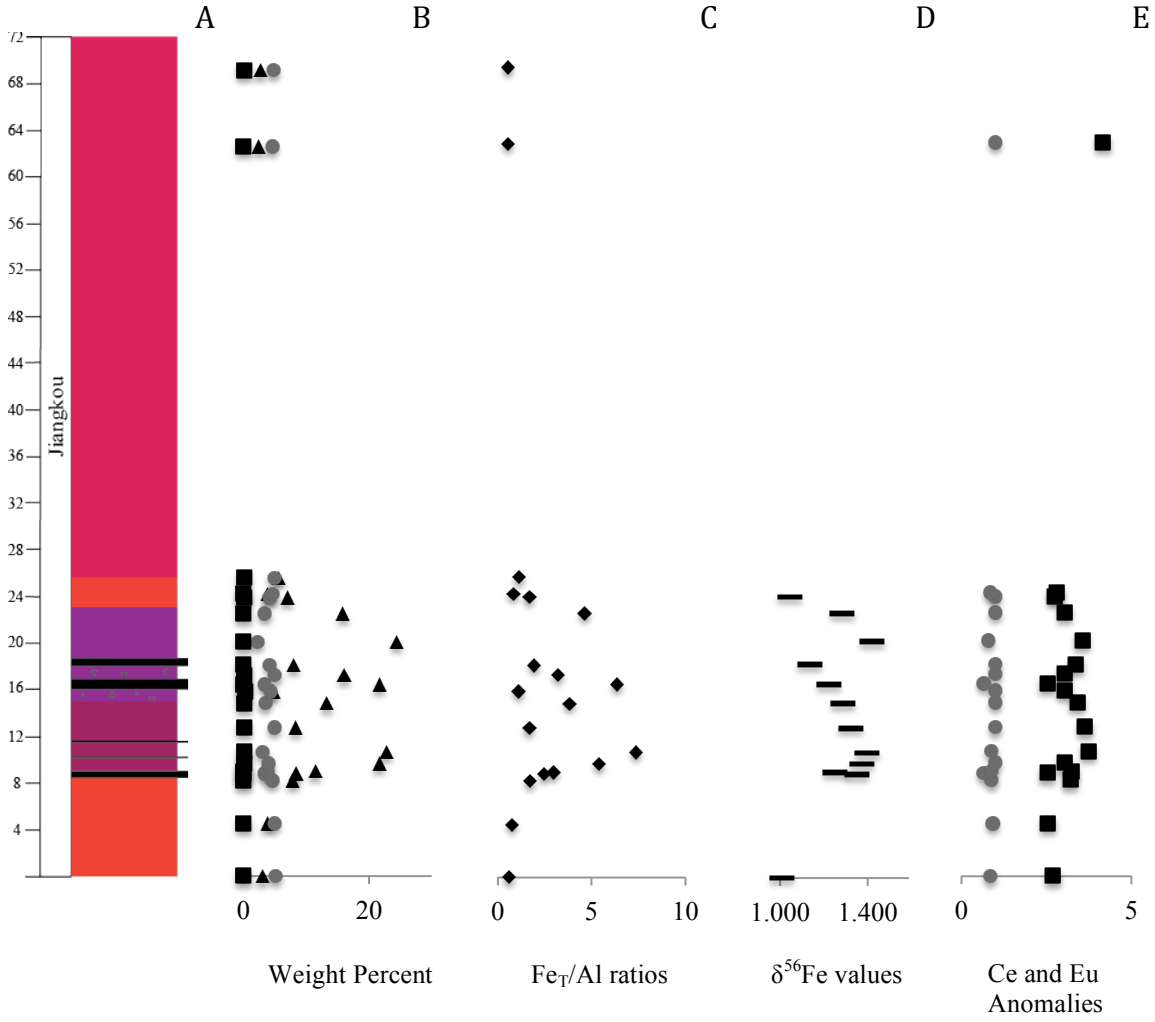

Figure 5. (A) Stratigraphic column for the Jiangkou section; depth profile constant throughout each graph. (B) Elemental profiles by weight percent for Mn (black squares), Al (grey circles), and Fe (black triangles). (C) Fe_T/Al ratios (black diamonds) (D) $\delta^{56}Fe$ values (horizontal lines). (E) Ce anomaly values (grey circles) and Eu anomaly values (black squares).

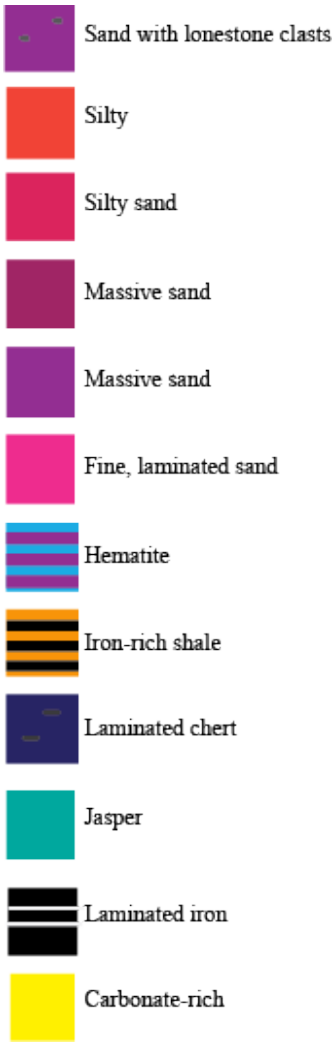

Figure 5.1. Legend of stratigraphic swatches for Figures 5A, 6A, and 7A.

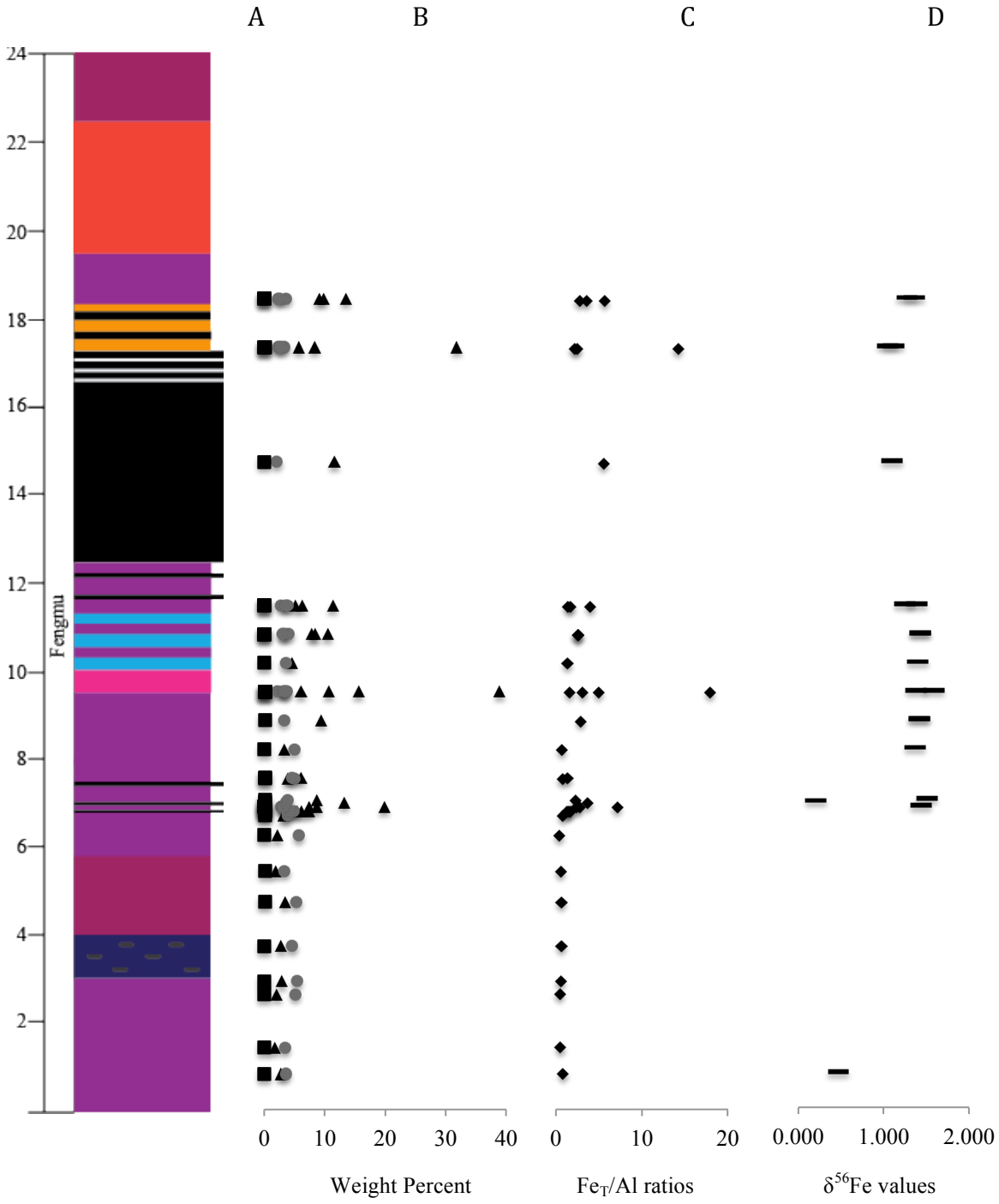

Figure 6. (A) Stratigraphic column for the Fengmu section; depth profile constant throughout each graph. (B) Elemental profiles by weight percent for Mn (black squares), Al (grey circles), and Fe (black diamonds). (C) Fe_T/Al ratios (black triangles) (D) δ^{56}Fe values (horizontal lines).

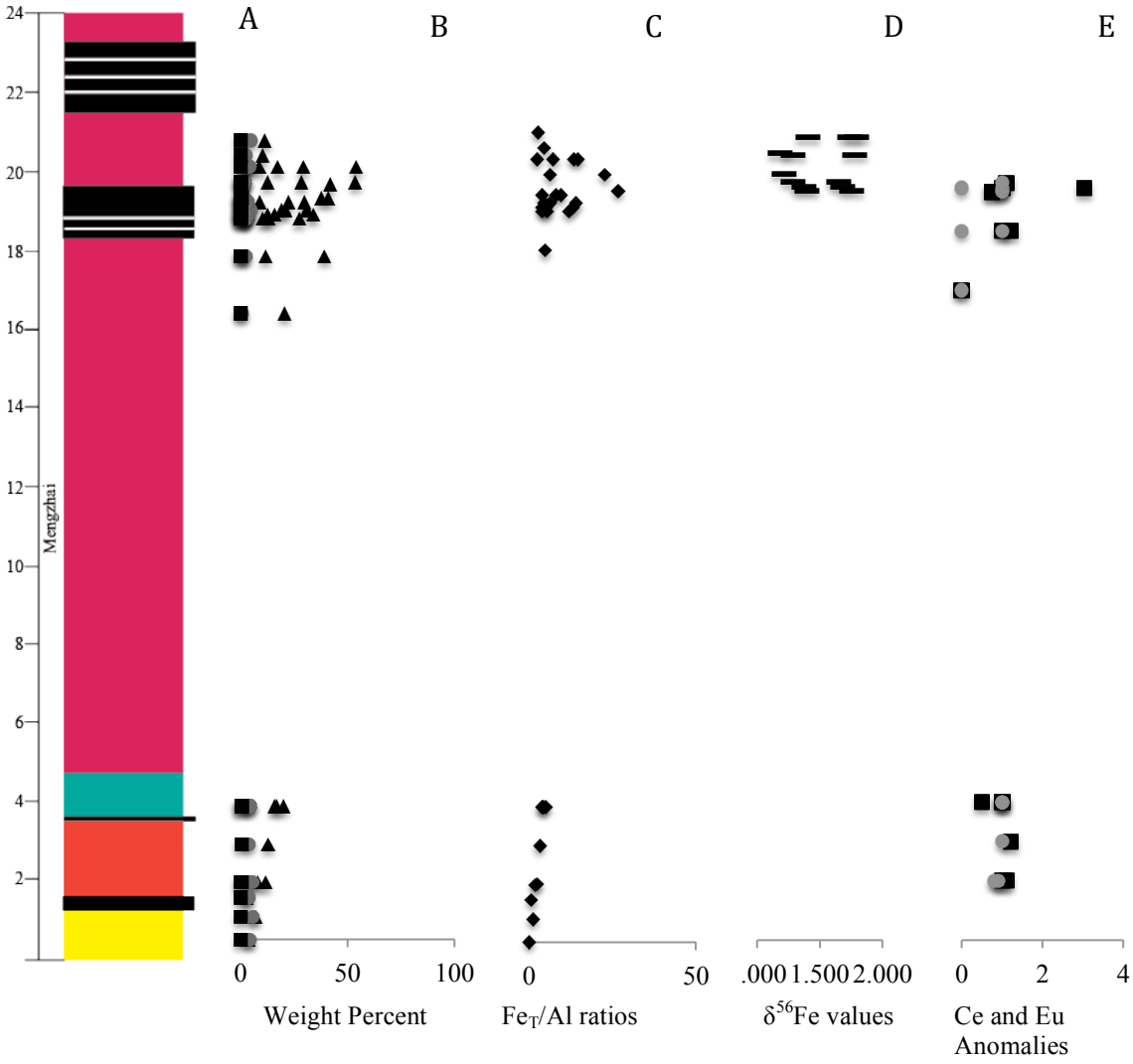

Figure 7. (A) Stratigraphic column for the Mengzhai section; depth profile constant throughout each graph. (B) Elemental profiles by weight percent for Mn (black squares), Al (grey circles), and Fe (black diamonds). (C) Fe_T/Al ratios (black diamonds). (D) $\delta^{56}Fe$ values (horizontal lines). (E) Ce anomaly values (grey circles) and Eu anomaly values (black squares).

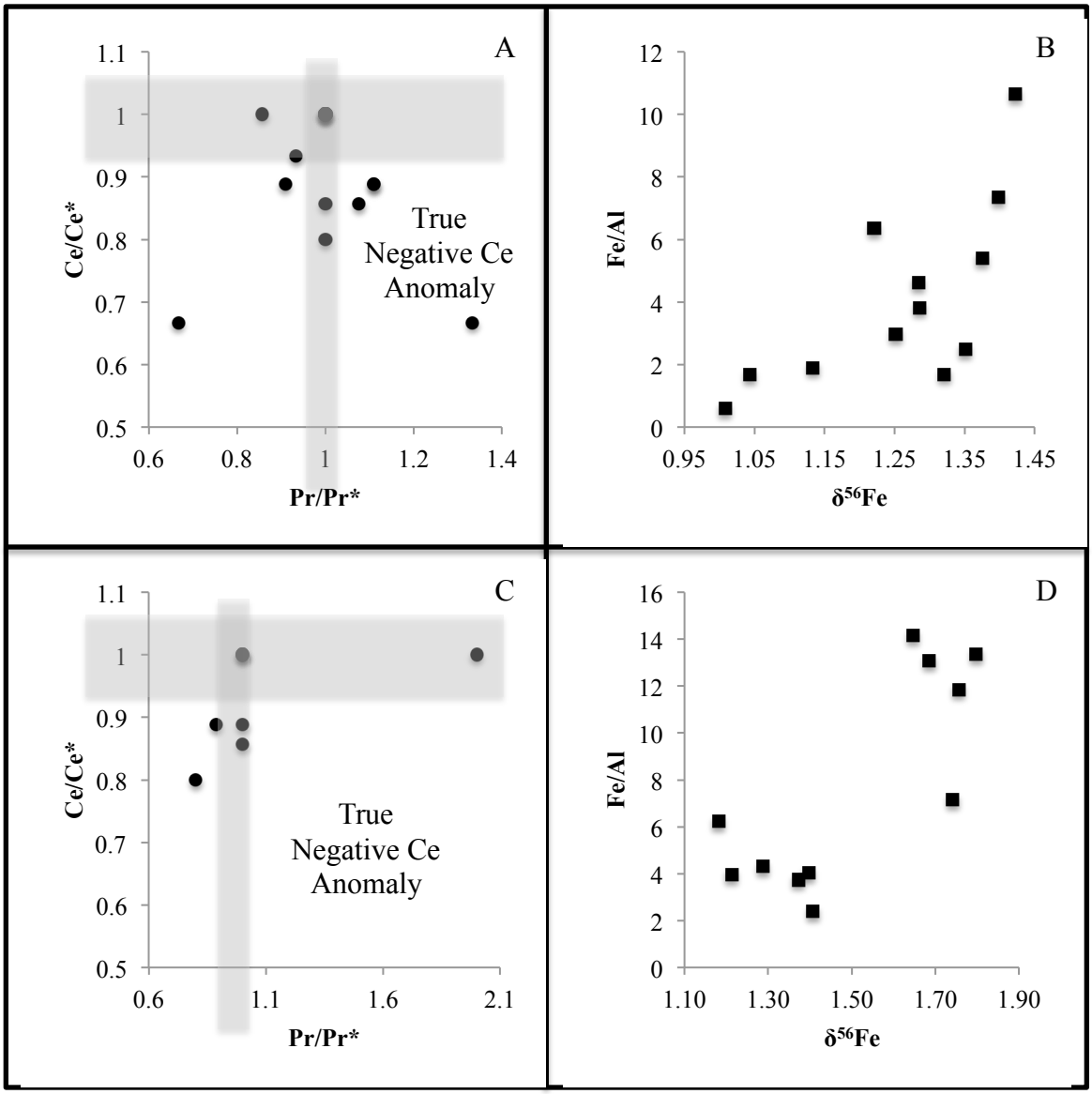

Figure 8. (A) Crossplot identifying true negative Ce anomalies for the Jiangkou section. True negative Ce anomalies are defined by Ce/Ce* ($Ce_{(SN)}/0.5Pr_{(SN)} + 0.5\ La_{(SN)}$) and ($Pr_{(SN)}/(0.5Ce_{(SN)} + 0.5Nd_{(SN)})$), as explained by Bau and Dulski (1996) and Planavsky et al. (2010). This method allow us to differentiate between positive La and true negative $Ce_{(SN)}$ anomalies (see text for details). (B) Crossplot revealing a positive correlation between Fe_T/Al and $\delta^{56}Fe$ values for the Jiangkou section. (C) Crossplot identifying true negative Ce anomalies for the Mengzhai section. (D) Crossplot revealing differences in Fe_T/Al and $\delta^{56}Fe$ values for iron-rich and iron-poor layers of samples from the Mengzhai section.

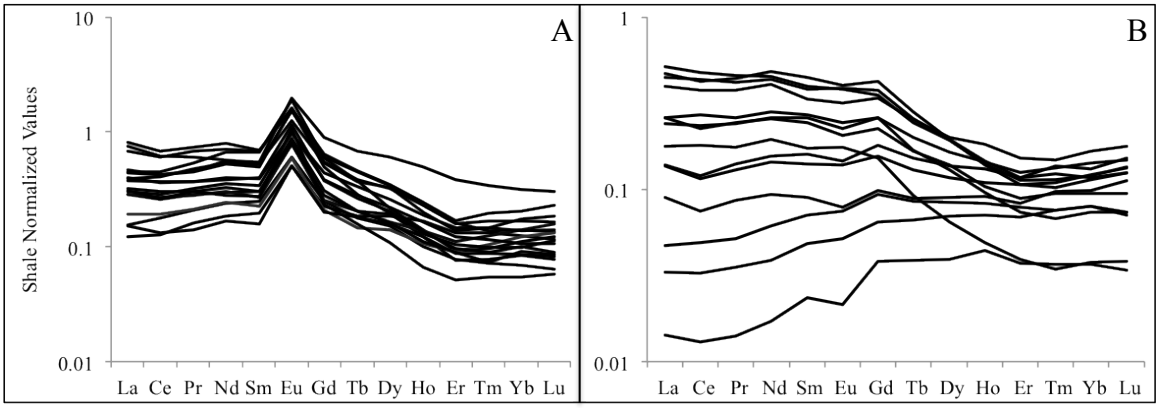

Figure 9. (A) Rare earth element pattern for the Jiangkou section; values are normalized to shale and plotted on a logarithmic scale. (B) Rare earth element pattern for the Mengzhai section; values are normalized to shale and plotted on a logarithmic scale.

References

Ali, K. A., Stern, R. J., Manton, W. I., Kimura, J. I., & Khamees, H. A. (2009). Geochemistry, Nd isotopes and U–Pb SHRIMP zircon dating of Neoproterozoic volcanic rocks from the Central Eastern Desert of Egypt: New insights into the~ 750Ma crust-forming event. *Precambrian Research*, *171*(1), 1-22.

Anbar, A. D. (2004). Iron stable isotopes: beyond biosignatures. *Earth and Planetary Science Letters*, *217*(3), 223-236.

Balci, N., Bullen, T. D., Witte-Lien, K., Shanks, W. C., Motelica, M., & Mandernack, K. W. (2006). Iron isotope fractionation during microbially stimulated Fe (II) oxidation and Fe (III) precipitation. *Geochimica et Cosmochimica Acta*, *70*(3), 622-639.

Baldwin, G. J., Turner, E. C., & Kamber, B. S. (2012). A new depositional model for glaciogenic Neoproterozoic iron formation: insights from the chemostratigraphy and basin configuration of the Rapitan iron formation 1 1 Northwest Territories Geoscience Office Contribution 0052. *Canadian Journal of Earth Sciences*, *49*(2), 455-476.

Basta, F. F., Maurice, A. E., Fontboté, L., & Favarger, P. Y. (2011). Petrology and geochemistry of the banded iron formation (BIF) of Wadi Karim and Um Anab, Eastern Desert, Egypt: implications for the origin of Neoproterozoic BIF.*Precambrian Research*, *187*(3), 277-292.

Bau, M., & Dulski, P. (1999). Comparing yttrium and rare earths in hydrothermal fluids from the Mid-Atlantic Ridge: implications for Y and REE behaviour during near-vent mixing and for the Y/Ho ratio of Proterozoic seawater. *Chemical Geology*, *155*(1), 77-90.

Bekker, A., Slack, J. F., Planavsky, N., Krapež, B., Hofmann, A., Konhauser, K. O., & Rouxel, O. J. (2010). Iron formation: the sedimentary product of a complex interplay among mantle, tectonic, oceanic, and biospheric processes.*Economic Geology*, *105*(3), 467-508.

Bergquist, B. A., Wu, J., & Boyle, E. A. (2007). Variability in oceanic dissolved iron is dominated by the colloidal fraction. *Geochimica et Cosmochimica Acta*,*71*(12), 2960-2974.

Bischoff, J. L., & Dickson, F. W. (1975). Seawater-basalt interaction at 200 C and 500 bars: implications for origin of sea-floor heavy-metal deposits and regulation of seawater chemistry. *Earth and Planetary Science Letters*, *25*(3), 385-397.

Bjerrum, C. J., & Canfield, D. E. (2002). Ocean productivity before about 1.9 Gyr ago limited by phosphorus adsorption onto iron oxides. *Nature*, *417*(6885), 159-162.

Boström, K., Peterson, M. N. A., Joensuu, O., & Fisher, D. E. (1969). Aluminum-poor ferromanganoan sediments on active oceanic ridges. *Journal of geophysical research*, *74*(12), 3261-3270.

Bowers, T. S., & Taylor, H. P. (1985). An integrated chemical and stable-isotope model of the origin of Midocean Ridge Hot Spring Systems. *Journal of Geophysical Research: Solid Earth (1978–2012)*, *90*(B14), 12583-12606.

Byrne R. H. and Sholkovitz E. R. (1996) Marine chemistry and geochemistry of the lanthanides. In Handbook on the Physics and Chemistry of Rare Earths(eds. K. A. Gschneidner, Jr. and L. Eyring), Vol. 23, pp. 497–593. Elsevier, Amsterdam.

Canfield, D. E. (2004). The evolution of the Earth surface sulfur reservoir.*American Journal of Science*, *304*(10), 839-861.

Canfield, D. E., Poulton, S. W., Knoll, A. H., Narbonne, G. M., Ross, G., Goldberg, T., & Strauss, H. (2008). Ferruginous conditions dominated later Neoproterozoic deep-water chemistry. *Science*, *321*(5891), 949-952.

Cloud, P. (1973). Paleoecological significance of the banded iron-formation.*Economic Geology*, *68*(7), 1135-1143.

Cox, G. M., Halverson, G. P., Minarik, W. G., Le Heron, D. P., Macdonald, F. A., Bellefroid, E. J., & Strauss, J. V. (2013). Neoproterozoic iron formation: An evaluation of its temporal, environmental and tectonic significance. *Chemical Geology*, *362*, 232-249.

Croal, L. R., Johnson, C. M., Beard, B. L., & Newman, D. K. (2004). Iron isotope fractionation by Fe (II)-oxidizing photoautotrophic bacteria. *Geochimica et cosmochimica acta*, *68*(6), 1227-1242.

Crosby, H. A., Johnson, C. M., Roden, E. E., & Beard, B. L. (2005). Coupled Fe (II)-Fe (III) electron and atom exchange as a mechanism for Fe isotope fractionation during dissimilatory iron oxide reduction. *Environmental science & technology*, *39*(17), 6698-6704.

Derry, L. A., & Jacobsen, S. B. (1990). The chemical evolution of Precambrian seawater: Evidence from REEs in banded iron formations. *Geochimica et Cosmochimica Acta*, *54*(11), 2965-2977.

Eisbacher, G.H., 1985. Late Proterozoic rifting, glacial sedimentation, and sedimentary cycles in the light of Windermere deposition. Palaeogeography, Palaeoclimatology, Palaeoecology 51, 231–254.

Elderfield, H., McCaffrey, R. J., Luedtke, N., Bender, M., & Truesdale, V. W. (1981). Chemical diagenesis in Narragansett Bay sediments. *American Journal of Science*, *281*(8), 1021-1055.

Elderfield, H., & Greaves, M. J. (1982). The rare earth elements in seawater.*Nature*, *296*, 214-219.

Elderfield, H., Whitfield, M., Burton, J. D., Bacon, M. P., & Liss, P. S. (1988). The oceanic chemistry of the rare-earth elements [and discussion].*Philosophical Transactions of the Royal Society of London. Series A, Mathematical and Physical Sciences*, *325*(1583), 105-126.

Fryer, B. J., & Taylor, R. P. (1987). Rare-earth element distributions in uraninites: implications for ore genesis. *Chemical Geology*, *63*(1), 101-108.

Garrels, J. I., & Gibson, W. (1976). Identification and characterization of multiple forms of actin. *Cell*, *9*(4), 793-805.

Gates, A. E., & Volkert, R. A. (2004). Vestiges of an Iapetan rift basin in the New Jersey Highlands: implications for the Neoproterozoic Laurentian margin.*Journal of Geodynamics*, *37*(3), 381-409.

German, C. R., & Elderfield, H. (1990). Application of the Ce anomaly as a paleoredox indicator: the ground rules. *Paleoceanography*, *5*(5), 823-833.

German, C. R., Holliday, B. P., & Elderfield, H. (1991). Redox cycling of rare earth elements in the suboxic zone of the Black Sea. *Geochimica et Cosmochimica Acta*, *55*(12), 3553-3558.

Gurvich, E. G. (2006). *Metalliferous sediments of the world ocean*. Berlin: Springer.

Halverson, G. P., Poitrasson, F., Hoffman, P. F., Nédélec, A., Montel, J. M., & Kirby, J. (2011). Fe isotope and trace element geochemistry of the Neoproterozoic syn-glacial Rapitan iron formation. *Earth and Planetary Science Letters*, *309*(1), 100-112.

Harland, W. B. (1964). Critical evidence for a great infra-Cambrian glaciation.*Geologische Rundschau*, *54*(1), 45-61.

Hartman, H. (1984). The evolution of photosynthesis and microbial mats: A speculation on the banded iron formations. *MBL LECT. BIOL. 1984.*

Hoffman, P. F., Kaufman, A. J., Halverson, G. P., & Schrag, D. P. (1998). A Neoproterozoic snowball earth. *Science*, *281*(5381), 1342-1346.

Hoffman, P. F. (1999). The break-up of Rodinia, birth of Gondwana, true polar wander and the snowball Earth. *Journal of African Earth Sciences*, *28*(1), 17-33.

Hoffman, P. F., & Schrag, D. P. (2002). The snowball Earth hypothesis: testing the limits of global change. *Terra Nova*, *14*(3), 129-155.

Hoffman, P. F., & Halverson, G. P. (2011). Neoproterozoic glacial record in the Mackenzie Mountains, northern Canadian Cordillera. *Geological Society, London, Memoirs*, *36*(1), 397-412.

Hurtgen, M. T., Arthur, M. A., Suits, N. S., & Kaufman, A. J. (2002). The sulfur isotopic composition of Neoproterozoic seawater sulfate: implications for a snowball Earth?. *Earth and Planetary Science Letters*, *203*(1), 413-429.

Isley, A. E. (1995). Hydrothermal plumes and the delivery of iron to banded iron formation. *The Journal of Geology*, 169-185.

Isley, A. E., & Abbott, D. H. (1999). Plume-related mafic volcanism and the deposition of banded iron formation. *Journal of Geophysical Research: Solid Earth (1978–2012)*, *104*(B7), 15461-15477.

Jiafu, T., Heqin, F., Zhqing, Y. (1987) Stratigraphy, Type and Formation Conditions of the Late Precambrian Banded Iron Ores in South China. *Geochemistry*, *6*(4), 331-3341.

Johnson, C. M., Skulan, J. L., Beard, B. L., Sun, H., Nealson, K. H., & Braterman, P. S. (2002). Isotopic fractionation between Fe (III) and Fe (II) in aqueous solutions. *Earth and Planetary Science Letters*, *195*(1), 141-153.

(a) Johnson, C. M., Beard, B. L., Klein, C., Beukes, N. J., & Roden, E. E. (2008). Iron isotopes constrain biologic and abiologic processes in banded iron formation genesis. *Geochimica et Cosmochimica Acta*, *72*(1), 151-169.

(b) Johnson, C. M., Beard, B. L., & Roden, E. E. (2008). The iron isotope fingerprints of redox and biogeochemical cycling in modern and ancient Earth.*Annu. Rev. Earth Planet. Sci.*, *36*, 457-493.

Kamber, B. S., & Webb, G. E. (2001). The geochemistry of late Archaean microbial carbonate: implications for ocean chemistry and continental erosion history. *Geochimica et Cosmochimica Acta*, *65*(15), 2509-2525.

Klein, C. (2005). Some Precambrian banded iron-formations (BIFs) from around the world: Their age, geologic setting, mineralogy, metamorphism, geochemistry, and origins. *American Mineralogist*, *90*(10), 1473-1499.

Kirschvink, J. L. (1992). Late Proterozoic low-latitude global glaciation: the snowball Earth.

Klein, C., & Beukes, N. J. (1993). Sedimentology and geochemistry of the glaciogenic late Proterozoic Rapitan iron-formation in Canada. *Economic Geology*, *88*(3), 542-565.

Klein, C., & Ladeira, E. A. (2004). Geochemistry and mineralogy of Neoproterozoic banded iron-formations and some selected, siliceous manganese formations from the Urucum District, Mato Grosso do Sul, Brazil.*Economic Geology*, *99*(6), 1233-1244.

Klinkhammer, G., Elderfield, H., & Hudson, A. (1983). Rare earth elements in seawater near hydrothermal vents.

Konhauser, K. O., Hamade, T., Raiswell, R., Morris, R. C., Ferris, F. G., Southam, G., & Canfield, D. E. (2002). Could bacteria have formed the Precambrian banded iron formations?. *Geology*, *30*(12), 1079-1082.

Konhauser, K. O., Newman, D. K., & Kappler, A. (2005). The potential significance of microbial Fe (III) reduction during deposition of Precambrian banded iron formations. *Geobiology*, *3*(3), 167-177.

Konhauser, K. O., Amskold, L., Lalonde, S. V., Posth, N. R., Kappler, A., & Anbar, A. (2007). Decoupling photochemical Fe (II) oxidation from shallow-water BIF deposition. *Earth and Planetary Science Letters*, *258*(1), 87-100.

Konhauser, K. O., Pecoits, E., Lalonde, S. V., Papineau, D., Nisbet, E. G., Barley, M. E., ... & Kamber, B. S. (2009). Oceanic nickel depletion and a methanogen famine before the Great Oxidation Event. *Nature*, *458*(7239), 750-753.

Kump, L. R., & Seyfried Jr, W. E. (2005). Hydrothermal Fe fluxes during the Precambrian: effect of low oceanic sulfate concentrations and low hydrostatic pressure on the composition of black smokers. *Earth and Planetary Science Letters*, *235*(3), 654-662.

Li, Z. X., Evans, D. A. D., & Zhang, S. (2004). A 90 spin on Rodinia: possible causal links between the Neoproterozoic supercontinent, superplume, true polar wander and low-latitude glaciation. *Earth and Planetary Science Letters*, *220*(3), 409-421.

Li, Z. X., Zhang, L., & Powell, C. M. (1995). South China in Rodinia: part of the missing link between Australia–East Antarctica and Laurentia?. *Geology*, *23*(5), 407-410.

Li, Z. X., Bogdanova, S. V., Collins, A. S., Davidson, A., De Waele, B., Ernst, R. E., ... & Vernikovsky, V. (2008). Assembly, configuration, and break-up history of Rodinia: a synthesis. *Precambrian Research*, *160*(1), 179-210.

Li, W., Huberty, J. M., Beard, B.L., Kita, N. T., Valley, J. W., Johnson, C. M. (2013) Contrasting behavior of oxygen and iron isotopes in banded iron formations revealed by *in situ* isotopic analysis. *Earth and Planetary Science Letters*, *384*(3), 132-143

Lottermoser, B. G., & Ashley, P. M. (2000). Geochemistry, petrology and origin of Neoproterozoic ironstones in the eastern part of the Adelaide geosyncline, South Australia. *Precambrian Research*, *101*(1), 49-67.

Lyons, T. W., Werne, J. P., Hollander, D. J., & Murray, R. W. (2003). Contrasting sulfur geochemistry and Fe/Al and Mo/Al ratios across the last oxic-to-anoxic transition in the Cariaco Basin, Venezuela. *Chemical Geology*,*195*(1), 131-157.

Lyons, T. W., & Severmann, S. (2006). A critical look at iron paleoredox proxies: New insights from modern euxinic marine basins. *Geochimica et Cosmochimica Acta*, *70*(23), 5698-5722.

Lyons, T. W., Reinhard, C. T., & Planavsky, N. J. (2014). The rise of oxygen in Earth/'s early ocean and atmosphere. *Nature*, *506*(7488), 307-315.

Michard, A., Albarede, F., Michard, G., Minster, J. F., & Charlou, J. L. (1983). Rare-earth elements and uranium in high-temperature solutions from East Pacific Rise hydrothermal vent field (13 N). *Nature*, *303*(5920), 795-797.

Mitra, A., Elderfield, H., & Greaves, M. J. (1994). Rare earth elements in submarine hydrothermal fluids and plumes from the Mid-Atlantic Ridge. *Marine Chemistry*, *46*(3), 217-235.

Olivarez, A. M., & Owen, R. M. (1989). REE/Fe variations in hydrothermal sediments: Implications for the REE content of seawater. *Geochimica et Cosmochimica Acta*, *53*(3), 757-762.

Olivarez, A. M., & Owen, R. M. (1991). The europium anomaly of seawater: implications for fluvial versus hydrothermal REE inputs to the oceans.*Chemical geology*, *92*(4), 317-328.

Piper, D. Z. (1974). Rare earth elements in the sedimentary cycle: a summary.*Chemical Geology*, *14*(4), 285-304.

Planavsky, N., Bekker, A., Rouxel, O. J., Kamber, B., Hofmann, A., Knudsen, A., & Lyons, T. W. (2010). Rare earth element and yttrium compositions of Archean and Paleoproterozoic Fe formations revisited: new perspectives on the significance and mechanisms of deposition. *Geochimica et Cosmochimica Acta*, *74*(22), 6387-6405.

Planavsky, N. J., McGoldrick, P., Scott, C. T., Li, C., Reinhard, C. T., Kelly, A. E., ... & Lyons, T. W. (2011). Widespread iron-rich conditions in the mid-Proterozoic ocean. *Nature*, *477*(7365), 448-451.

Poulton, S. W., & Canfield, D. E. (2011). Ferruginous conditions: a dominant feature of the ocean through Earth's history. *Elements*, *7*(2), 107-112.

Powell, C. M., Preiss, W. V., Gatehouse, C. G., Krapez, B., & Li, Z. X. (1994). South Australian record of a Rodinian epicontinental basin and its mid-Neoproterozoic breakup (~ 700 Ma) to form the Palaeo-Pacific Ocean.*Tectonophysics*, *237*(3), 113-140.

Preiss, W. V. (2000). The Adelaide Geosyncline of South Australia and its significance in Neoproterozoic continental reconstruction. *Precambrian Research*, *100*(1), 21-63.

Raiswell, R., Newton, R., Bottrell, S. H., Coburn, P. M., Briggs, D. E., Bond, D. P., & Poulton, S. W. (2008). Turbidite depositional influences on the diagenesis of Beecher's Trilobite Bed and the Hunsrück Slate; sites of soft tissue pyritization. *American Journal of Science*, *308*(2), 105-129.

Raiswell, R., & Canfield, D. E. (2012). The iron biogeochemical cycle past and present. *Geochemical Perspectives*, *1*(1), 1-322.

Rooney, A. D., Macdonald, F. A., Strauss, J. V., Dudás, F. Ö., Hallmann, C., & Selby, D. (2014). Re-Os geochronology and coupled Os-Sr isotope constraints on the Sturtian snowball Earth. *Proceedings of the National Academy of Sciences*, *111*(1), 51-56.

Rouxel, O. J., Bekker, A., & Edwards, K. J. (2005). Iron isotope constraints on the Archean and Paleoproterozoic ocean redox state. *Science*, *307*(5712), 1088-1091.

Ruhlin, D. E., & Owen, R. M. (1986). The rare earth element geochemistry of hydrothermal sediments from the East Pacific Rise: Examination of a seawater scavenging mechanism. *Geochimica et Cosmochimica Acta*, *50*(3), 393-400.
Sahoo, S. K., Planavsky, N. J., Kendall, B., Wang, X., Shi, X., Scott, C., ... & Jiang, G. (2012). Ocean oxygenation in the wake of the Marinoan glaciation.*Nature*, *489*(7417), 546-549.

Severmann, S., Johnson, C. M., Beard, B. L., German, C. R., Edmonds, H. N., Chiba, H., & Green, D. R. H. (2004). The effect of plume processes on the Fe isotope composition of hydrothermally derived Fe in the deep ocean as inferred from the Rainbow vent site, Mid-Atlantic Ridge, 36 14′ N. *Earth and Planetary Science Letters*, *225*(1), 63-76.

Severmann, S., Lyons, T. W., Anbar, A., McManus, J., & Gordon, G. (2008). Modern iron isotope perspective on the benthic iron shuttle and the redox evolution of ancient oceans. *Geology*, *36*(6), 487-490.

Sial, A. N., Campos, M. S., Gaucher, C., Frei, R., Ferreira, V. P., Nascimento, R. C., Pimentel, M. M., & Pereira, N. S. (2014). Algoma-Type Neoproterozoic BIFs and Related Marbles in the Seridó Belt (NE Brazil): REE, C, O, Cr and Sr Isotope Evidence. *Goldschmidt Abstracts*, 2303.

Staton, S., Amskold, L., Gordon, G., Anbar, A., & Konhauser, K. (2006, May). Iron isotope fractionation during photo-oxidation of aqueous ferrous iron. In*AGU Spring Meeting Abstracts* (Vol. 1, p. 04).

Sverjensky, D. A. (1984). Europium redox equilibria in aqueous solution. *Earth and Planetary Science Letters*, *67*(1), 70-78.

Swanson-Hysell, N. L., Rose, C. V., Calmet, C. C., Halverson, G. P., Hurtgen, M. T., & Maloof, A. C. (2010). Cryogenian glaciation and the onset of carbon-isotope decoupling. *Science*, *328*(5978), 608-611.

Tang, J., Fu, H., & Yu, Z. (1987). Stratigraphy, type and formation conditions of the Late Precambrian banded iron ores in South China. *Chinese Journal of Geochemistry*, *6*(4), 331-341.

Volkert, R. A., Monteverde, D. H., Friehauf, K. C., Gates, A. E., Dalton, R. F., & Smith, R. C. (2010). Geochemistry and origin of Neoproterozoic ironstone deposits in the New Jersey Highlands and implications for the eastern Laurentian rifted margin in the north-central Appalachians, USA. *Geological Society of America Memoirs*, *206*, 283-306.

Wang, J., & Li, Z. X. (2003). History of Neoproterozoic rift basins in South China: implications for Rodinia break-up. *Precambrian Research*, *122*(1), 141-158.

Young, G. M. (1976). Iron-formation and glaciogenic rocks of the Rapitan Group, Northwest Territories, Canada. *Precambrian Research*, *3*(2), 137-158.

Zhang, Q. R., Li, X. H., Feng, L. J., Huang, J., & Song, B. (2008). A new age constraint on the onset of the Neoproterozoic glaciations in the Yangtze Platform, South China. *The Journal of Geology*, *116*(4), 423-429.

Zhang, Q-R, Chu, X-L, & Feng, L-J. (2011). Chapter 32 Neoproterozoic glacial records in the Yangtze region, China. Geological Society, London, Memoirs. 36, 357-366.

Appendices

Sample	depth	d56/54Fe	Fe/Al	Fe ppm in rock	Boiling HCl (% reactive iron)	Reactive to total	Mg ppm in rock	Ca ppm in rock	Al ppm in rock	P ppm in rock	Ti ppm in rock	V ppm in rock	Cr ppm in rock	Mn ppm in rock	Mo ppm in rock	La	Ce	Pr	Nd	Sm	Eu	Gd	Tb	Dy	Ho	Er	Tm	Yb	Lu	Ce anomaly (Planavsky)	Eu anomaly (Planavsky)	Pr anomaly (Planavsky)
SCF1-1	8.2		1.7	78456	6	74	8691	15	45999	320	214	53	26	502	1	0.4	0.4	0.5	0.7	0.7	1.9	0.6	0.4	0.2	0.1	0.1	0.1	0.1	0.1	0.9	3.2	0.9
SCF1-2	4.5		0.8	37766	0	11	7309	26	48783	247	256	55	30	368	1	0.8	0.7	0.7	0.8	0.7	1.6	0.6	0.5	0.3	0.2	0.2	0.2	0.2	0.2	0.9	2.6	0.9
SCF1-3	0	1.008	0.6	29971	1	50	8664	47	50622	233	178	49	26	266	1	0.7	0.6	0.7	0.7	0.7	1.6	0.6	0.4	0.3	0.2	0.2	0.2	0.2	0.2	0.9	2.7	1.1
SCF1-4	8.8	1.351	2.5	83389	1	10	5632	105	33673	954	220	55	26	279	1	0.1	0.1	0.2	0.2	0.2	0.5	0.2	0.2	0.2	0.2	0.1	0.1	0.1	0.1	0.7	2.5	1.3
SCF1-5	9	1.252	3.0	114581	10	90	8350	283	38737	2232	264	63	46	505	1	0.4	0.4	0.5	0.5	0.5	1.5	0.5	0.4	0.3	0.2	0.2	0.1	0.1	0.1	0.9	3.2	1.1
SCF1-6	9.7	1.375	5.4	216459	0	2	13008	100	40098	716	215	81	42	848	1	0.2	0.2	0.2	0.2	0.2	0.6	0.2	0.2	0.2	0.1	0.1	0.1	0.1	0.1	1.0	3.0	1.0
SCF1-7	10.65	1.398	7.4	227213			13467	70	30876	494	254	70	64	858	2	0.4	0.4	0.5	0.5	0.5	1.6	0.5	0.3	0.2	0.1	0.1	0.1	0.1	0.1	0.9	3.7	1.1
SCF1-8	12.75	1.321	1.7	82666	8	96	6787	50	49213	722	219	50	26	875	1	0.2	0.2	0.2	0.2	0.2	0.6	0.2	0.1	0.1	0.1	0.1	0.1	0.1	0.1	1.0	3.6	1.0
SCF1-9	14.85	1.286	3.8	133027	1	9	7229	777	34785	1013	199	59	23	798	1	0.3	0.3	0.3	0.3	0.3	0.9	0.3	0.2	0.2	0.1	0.1	0.1	0.1	0.1	1.0	3.4	1.0
SCF1-10	15.85		1.1	46908	2	42	4880	67	43114	792	179	40	16	1831	1	0.3	0.3	0.3	0.3	0.3	0.8	0.3	0.2	0.2	0.1	0.1	0.1	0.1	0.2	1.0	3.0	1.0
SCF1-11	16.45	1.221	6.4	216128			7517	151	34018	1233	235	86	30	366	1	0.2	0.1	0.1	0.2	0.2	0.5	0.2	0.2	0.2	0.1	0.1	0.1	0.1	0.1	0.7	2.5	0.7
SCF1-12	17.27		3.2	160310			10315	1085	49997	995	198	70	27	1060	1	0.3	0.3	0.3	0.3	0.3	0.8	0.3	0.2	0.2	0.1	0.1	0.1	0.1	0.1	1.0	3.0	1.0
SCF1-13	18.12	1.133	1.9	79391			5107	86	41637	755	194	63	29	171	1	0.3	0.3	0.3	0.4	0.3	1.0	0.4	0.3	0.2	0.2	0.1	0.1	0.1	0.1	1.0	3.4	0.9
SCF1-14	20.12	1.422	10.6	243591	1	6	4828	309	22882	2514	162	67	28	478	1	0.5	0.4	0.5	0.6	0.5	2.0	0.9	0.7	0.6	0.5	0.4	0.3	0.3	0.3	0.8	3.6	1.0
SCF1-15	22.52	1.284	4.6	157917			6838	181	34161	1136	169	62	24	497	1	0.4	0.4	0.4	0.4	0.4	1.1	0.4	0.3	0.2	0.1	0.1	0.1	0.1	0.1	1.0	3.0	1.0
SCF1-16	23.92	1.043	1.7	69828	5	71	6029	73	41813	364	201	75	27	1011	1	0.4	0.4	0.4	0.4	0.4	1.0	0.4	0.3	0.3	0.2	0.1	0.1	0.2	0.2	1.0	2.8	1.0
SCF1-17	24.22		0.8	38493	3	78	6215	55	46436	433	274	81	31	379	1	0.8	0.6	0.6	0.6	0.5	1.3	0.5	0.4	0.3	0.2	0.1	0.1	0.1	0.1	0.9	2.8	1.0
SCF 1-18			1.1	56603	5	94	9012	95	49348	574	303	82	40	766	1																		
SCF1-19	62.62		0.5	25075	1	41	4052	15	45832	-28	179	58	13	316	1	0.3	0.3	0.3	0.3	0.3	1.1	0.2	0.2	0.1	0.1	0.1	0.1	0.1	0.1	1.0	4.2	1.0
SCF 1-20			0.6	27010	2	81	7419	491	48478	103	223	60	13	905	1																		

Sample	depth	d56/54Fe	Fe/Al	Fe ppm in rock	Boiling HCl (% reactive iron)	Reactive to total	Mg ppm in rock	Ca ppm in rock	Al ppm in rock	P ppm in rock	Ti ppm in rock	V ppm in rock			
SCF 2-1	0.8	0.472	1	28244			5065	28	35031	75	150	37	19	361	2
SCF 2-2	1.4		1	17455	0.9	51.3	4658	42	34656	77	133	27	16	283	1
SCF 2-3	2.6		0	21131	1.4	66.3	5692	53	51216	164	209	41	25	284	1
SCF 2-4	2.9		1	29131	1.6	55.9	7294	44	54366	187	173	41	20	394	1
SCF 2-4	3.7		1	28055			6761	76	46499	158	173	42	19	373	1
SCF 2-6	4.7		1	34527	2.4	68.3	8811	27	53003	126	231	42	22	519	1
SCF 2-7	5.4		1	18787	0.9	47.4	5129	214	33583	105	153	21	18	1373	1
SCF 2-8	6.2		0	21791	0.8	36.3	6184	56	56841	170	184	38	21	306	1
SCF 2-9	6.65		1	32036	1.2	36.4	7383	62	38683	178	154	30	20	708	1
SCF 2-10 A	6.75		2	74336			15581	45	49054	293	167	33	21	838	1
SCF 2-10 B	6.75		2	61625			9977	32	37716	132	195	39	46	618	1
SCF 2-10 Bulk	6.75		1	54087	4.0	74.9	12452	41	43354	213	199	29	26	861	1
SCF 2-11 A	6.85	1.438	7	198487			4228	32	27741	172	427	97	57	357	3
SCF 2-11 B	6.85		3	86662			4100	27	31834	136	186	58	25	259	1
SCF 2-11 Bulk	6.85		2	74149			4590	30	31620	192	155	51	25	283	1
SCF 2-12	6.95	0.209	4	132335	12.9	97.5	9295	36	36103	192	235	58	29	522	1
SCF 2-13 A	7	1.501													
SCF 2-13 B	7														
SCF 2-13 Bulk	7		2	87264			8372	18	38580	223	109	50	22	541	1
SCF 2-14	7.5		1	39059			9032	48	50144	258	207	38	23	436	1
SCF 2-15	7.506		1	60592			15167	29	44921	214	111	37	19	1250	1
SCF 2-16	8.156	1.372	1	32898	1.6	50.1	7678	45	49832	298	171	52	28	313	1
SCF 2-17 Bulk	8.806		3	94373			5439	26	32902	233	233	62	54	493	1
SCF 2-17 A	8.806	1.421													
SCF 2-17 B	8.806	1.417													
SCF 2-18 A	9.456		2	60421	4.8	79.0	8877	35	37539	246	73	41	27	504	1
SCF 2-18 B	9.456	1.591	18	388884			5267	5	21681	141	809	191	45	631	1
SCF 2-18 C	9.456	1.383	5	155701			9507	13	31317	138	270	75	50	927	1
SCF 2-18 Bulk	9.456		3	106797			8455	10	34407	219	190	61	35	735	1
SCF 2-19	10.106	1.405	1	45620			4262	27	35103	242	168	45	26	285	2
SCF 2-20 A	10.756	1.428	3	84438	0.9	10.2	6782	23	32558	207	170	51	29	305	1
SCF 2-20 B	10.756	1.425	3	105261	7.7	73.1	8251	25	41176	229	223	62	30	397	1
SCF 2-20 Bulk	10.756		3	78852			6547	21	30976	175	155	48	25	402	1
SCF 2-21 A	11.406	1.390	1	52083	9.7	186.2	7138	22	38184	273	109	44	31	343	1
SCF 2-21 B	11.406	1.245	4	113664	9.4	83.1	6197	5	28513	96	293	66	61	370	1
SCF 2-21 Bulk	11.406		2	62581			6172	13	35969	210	173	49	37	319	1
SCF 2-23		1.280													
SCF 2-24	14.656	1.101	6	116009			8573	35	20924	304	133	38	23	179	1
SCF 2-25 A	17.256	1.051	2	83184			6578	29	33312	109	198	63	57	120	1
SCF 2-25 B	17.256	1.122	14	317780			9559	93	22320	-55	442	107	135	476	4
SCF 2-25 Bulk	17.256		2	57340			4912	26	26897	179	138	46	36	100	1
SCF 2-26 A	18.356	1.273	3	98223			8157	50	35832	364	199	91	46	194	2
SCF 2-26 B	18.356	1.356	6	135279			6780	20	23894	80	291	89	68	167	1
SCF 2-26 Bulk	18.356		4	90242			6948	25	25165	157	191	67	62	165	1
SCF 2-31	24.12	0.432	1											100	

Sample	depth	d56/54Fe	Fe/Al	Fe ppm in rock	Boiling HCl (% reactive iron)	Reactive to total	Mg ppm in rock	Ca ppm in rock	Al ppm in rock							La	Ce	Pr	Nd	Sm	Eu	Gd	Tb	Dy	Ho	Er	Tm	Yb	Lu	Ce anomaly (Planavsky)	Eu anomaly (Planavsky)	Pr anomaly (Planavsky)
SCF 3-1	0	0.008		38306			4232	53	42789	272	248	57	24	427	1																	
SCF 3-2	0.6	-0.055	1.2	69070			6149	77	57351	259	454	87	41	758	2																	
SCF 3-3	1.1	0.126	0.8	30605	2.6	85.4	999	29	36501	224	206	65	22	242	1																	
SCF 3-4	1.5	-0.129	1.9	80248			1006	4	42324	316	255	60	26	903	1	0.5	0.4	0.4	0.5	0.4	0.4	0.4	0.3	0.2	0.1	0.1	0.1	0.1	0.1	0.9	1.1	0.9
SCF 3-5	1.51		2.2	115898			9355	47	52111	325	310	75	31	2106	2	0.3	0.2	0.2	0.3	0.2	0.2	0.2	0.2	0.1	0.1	0.1	0.1	0.1	0.1	0.8	1.0	0.8
SCF 3-6	2.51		3.2	126535			7080	103	39506	1103	276	73	33	3006	3	0.5	0.5	0.5	0.5	0.4	0.4	0.4	0.2	0.2	0.1	0.1	0.1	0.1	0.1	1	1.2	1.0
SCF 3-7A	3.51		3.9	157285			12164	78	40332	667	183	74	22	1707	1	0.1	0.1	0.1	0.2	0.2	0.1	0.2	0.2	0.1	0.1	0.1	0.1	0.1	0.2	1	0.5	0.7
SCF 3-7B	3.51		4.1	165822			12236	52	40321	536	259	85	22	1931	2	0.1	0.1	0.1	0.1	0.1	0.1	0.1	0.1	0.1	0.1	0.1	0.1	0.1	0.1	1	1.0	1.0
SCF 3-7 bulk	3.51		4.9	198873			12397	74	40718	701	230	94	23	2459	1	0.1	0.1	0.1	0.1	0.1	0.2	0.1	0.1	0.1	0.1	0.1	0.1	0.1	0.1	1	1.0	1.0
SCF 3-8	16.51			203391			358	25	3852	38	48	46	54	46	2	0.0	0.0	0.0	0.0	0.0	0.0	0.0	0.0	0.0	0.0	0.0	0.0	0.0	0.0	0	0.0	0.0
SCF 3-9A	18.01			393442			2328	54	5773	466	124	85	38	228	2	0.0	0.0	0.1	0.1	0.1	0.1	0.1	0.1	0.1	0.1	0.1	0.1	0.1	0.1	0	1.0	2.0
SCF 3-9B	18.01		4.7	116473			13166	50	24712	419	36	22	72	244	2	0.2	0.2	0.2	0.2	0.2	0.2	0.2	0.1	0.1	0.0	0.0	0.0	0.0	0.0	1	1.2	1.0
SCF 3-10A	19.01	1.757	11.9	273448			12151	17	23061	168	285	96	33	220	1	0.2	0.2	0.2	0.3	0.3	0.2	0.3	0.2	0.2	0.1	0.1	0.1	0.1	0.1	1	0.8	0.8
SCF 3-10B	19.01	1.397	4.1	104332			14760	30	25730	394	92	28	24	166	1																	
SCF 3-10 Bulk	19.01		5.5	129082			13533	30	23301	341	112	39	28	308	1	0.3	0.3	0.3	0.3	0.3	0.2	0.3	0.2	0.1	0.1	0.1	0.1	0.1	0.1	1	0.8	1.0
SCF 3-11 A	19.110	1.686	13.1	338158			14084	18	25820	172	429	126	37	391	2	0.0	0.0	0.0	0.0	0.0	0.1	0.1	0.1	0.1	0.1	0.1	0.1	0.1	0.1	0	3.0	0.0
SCF 3-11 B	19.110	1.372	3.7	124687			18766	35	33360	560	250	35	28	276	2																	
SCF 3-11 bulk	19.110		5.0	156165			17391	39	31061	308	200	47	29	446	1	0.4	0.4	0.4	0.4	0.3	0.3	0.3	0.2	0.2	0.2	0.1	0.2	0.2	1	1.0	1.0
SCF 3-12 A	19.23	1.289	4.3	209236			26598	13	48529	598	210	55	57	899	3																	
SCF 3-12 B	19.23	1.647	14.2	308060			11658	24	21764	89	398	115	40	340	2																	
SCF 3-12 Bulk	19.23		6.4	189838			16019	89	29878	335	173	58	47	793	1	0.4	0.4	0.4	0.4	0.4	0.4	0.4	0.3	0.2	0.1	0.1	0.1	0.1	0.1	1	1.1	1.0
SCF 3-13 A	19.45		9.5	298088			15928	103	31358	1022	338	113	27	257	2																	
SCF 3-13 B	19.45	1.213	3.9	89727			12941	6	22815	265	125	25	26	366	2																	
SCF 3-13 Bulk	19.45		7.9	223215			15145	79	28107	564	211	71	24	385	2																	
SCF 3-14 A	19.55			408827			2367	22	6642	276	224	127	48	1292	4																	
SCF 3-14 B	19.55			806724			12362	829	666	255	3	7	6	426	2																	
SCF 3-14 Bulk	19.55		26.8	376919			6546	21	14086	161	184	103	43	857	3																	
SCF 3-15 A	19.92	1.290																														
SCF 3-15 B	19.92	1.778																														
SCF 3-15 Bulk	19.92			416321			6725	196	10778	1553	208	99	46	261	2																	
SCF 3-16 AB	19.97	1.182	6.2	125942			11872	36	20244	286	90	32	59	375	2																	
SCF 3-16 Bulk	19.97		22.8	282274			7653	67	12404	359	184	74	47	163	1																	
SCF 3-16 C	19.97			533905			5535	51	10651	601	378	149	50	126	2																	
SCF 3-17 Bulk	20.37		14.7	290924			12010	137	19836	1193	146	70	29	278	2																	
SCF 3-17 A	20.37	1.741	7.1	172718			11222	213	24181																							
SCF 3-17 B	20.37	1.798	13.4	540017			23427	1731	40381																							
SCF 3-17 C	20.37	1.407	2.4	85796			22992	2065	36226																							
SCF 3-18	20.67		4.5	101905	6.0	59.0	14091	26	22634	230	51	24	36	288	1																	
SCF 3-19	21.07		2.6	113649	3.7	32.3	21811	25	43428	274	294	43	44	495	1																	